

7

## 3 Superelasticity and Shape Memory Behavior of NiTiHf Alloys

4 H. Sehitoglu<sup>1</sup> · Y. Wu<sup>1</sup> · L. Patriarca<sup>1,2</sup> · G. Li<sup>1</sup> · A. Ojha<sup>1</sup> · S. Zhang<sup>3</sup> ·  
5 Y. Chumlyakov<sup>4</sup> · M. Nishida<sup>5</sup>

6

7 © ASM International 2017

8 **Abstract** The NiTiHf high-temperature shape memory  
9 alloys represent a significant advancement in extending  
10 the functionality of binary NiTi to elevated temperatures  
11 above 100 °C. Despite this potential, the previous results  
12 in the literature point to a disappointingly low shape  
13 memory strains with addition of Hf. On the other hand,  
14 based on theoretical analysis using the lattice constants,  
15 the transformation strains should increase substantially  
16 with increase in Hf content. The present paper addresses  
17 this discrepancy, and using atomistic simulations, deter-  
18 mination of twinning modes in martensite with trans-  
19 mission electron microscopy, digital image measurements  
20 of habit plane orientation, and strains in single-crystal  
21 specimens show that the experimental transformation  
22 strains in NiTiHf indeed increase with increasing Hf to  
23 unprecedented strain levels near 20%. The Hf contents  
24 considered were in the range 6.25–25 at.%, and NiTi (0%  
25 Hf) results are provided as the baseline. The current work  
26 represents more than 60 experiments representing an

extremely thorough study on single crystals and 27  
polycrystals. 28

**Keywords** Superelasticity · Shape memory effect · 30  
Electron microscopy · Transformation strain · NiTiHf 31

**Introduction** 32

**Historical Background** 33

NiTi alloys are the most widely used shape memory alloys 34  
(SMAs) due to their superior superelastic and shape mem- 35  
ory behavior [1]. The NiTi possesses high transformation 36  
strains [2], low thermal and stress hysteresis [3], and good 37  
fatigue resistance [4]. The alloy has been a technological 38  
success with applications ranging from biomedical (mostly 39  
stents) to mechanical devices (such as actuators). Its 40  
behavior is well understood at the macro-level [5] and many 41  
issues at the micro-level are continuing to be investigated 42  
[6]. The NiTiHf alloys are relatively unexplored compared 43  
to NiTi, but have attracted considerable attention in the last 44  
10 years [7–15]. The NiTiHf exhibits excellent slip resis- 45  
tance [16, 17] and high transformation temperatures [18]. 46  
At this stage, the basic SMA properties of NiTiHf are still 47  
being determined and the results are found to be highly 48  
dependent on many factors such as composition, (Ni/Hf 49  
contents), heat treatments, aging to generate precipitates, 50  
test temperatures, tension versus compression, and dislo- 51  
cation slip resistance [7–15]. Early works on transformation 52  
strains focused on the addition of Hf in the range 15–20 53  
at.% [19, 20] were insightful. In this study, we show the 54  
functionality of the new NiTiHf ternary alloys with Hf 55  
contents as high as 25 at.%. 56

A1 ✉ H. Sehitoglu  
A2 huseyin@illinois.edu

A3 ✉ Y. Wu  
A4 yanwu7@illinois.edu

A5 <sup>1</sup> Department of Mechanical Science and Engineering,  
A6 University of Illinois at Urbana-Champaign, 1206 W. Green  
A7 Street, Urbana, IL 61801, USA

A8 <sup>2</sup> Department of Mechanical Engineering, Politecnico di  
A9 Milano, Via La Masa 1, 20156 Milan, Italy

A10 <sup>3</sup> Abbott Laboratories, Plymouth, MN 55311, USA

A11 <sup>4</sup> Tomsk State University, Tomsk, Russia

A12 <sup>5</sup> Department of Engineering Sciences for Electronics and  
A13 Materials, Faculty of Engineering Sciences, Kyushu  
A14 University, Kasuga, Fukuoka 816-8580, Japan

57 **Insight into NiTiHf Alloys**

58 The calculations of the transformation strain for the binary  
59 NiTi have been published in early works and compared  
60 with experiments with good overall agreement [2, 21–24].  
61 The highest transformation strains in binary NiTi have  
62 been observed as 10% in tension and 5.5% in compression.  
63 It is noteworthy that the theoretical transformation strains  
64 for NiTiHf are superior for both tension and compression  
65 compared to NiTi, while the asymmetry in tension–com-  
66 pression prevails. The strain increases linearly with Hf  
67 content [25], and so even small additions of Hf produce  
68 higher magnitudes of transformation strains. Since the  
69 NiTiHf transformation strains in compression can reach as  
70 high as 7% without the propensity of fracture, this can open  
71 up new applications. The tensile strains can reach near 15%  
72 which also exceeds the binary NiTi alloys (10%) and can  
73 find specific uses. In this paper, we provide the calculations  
74 of the transformation strains for the NiTiHf SMAs with  
75 different Hf compositions (as high as 25 at.%) to elucidate  
76 our point.

77 The use of the NiTi binary system is limited by its trans-  
78 formation temperature to below 75 °C. To increase the  
79 transformation temperature of the alloy to above 120 °C,  
80 ternary Hf elements can be added. With small additions of  
81 Hf, the transformation temperature may not exhibit an  
82 observable increase; however, above 15 at.% Hf, the trans-  
83 formation temperature changes becomes substantial and can  
84 reach 350 °C. Other ternary elements have been attempted to  
85 raise TTs, but Hf provides the best mechanical properties  
86 [7, 10, 18, 19, 26–33] such as slip resistance (>1 GPa) [16],  
87 reasonable cost (compared to Pd and Pt). The range of Hf can  
88 vary from less than 10 to as high as 25 at.% and can elevate  
89 the transformation temperatures from 75 to 400 °C. This  
90 increase can potentially open new applications.

91 **The Need for Present Work**

92 As stated above, previous papers postulated the potential  
93 niche role of NiTiHf alloys in the SMA field. Notwith-  
94 standing this promise, the experimental results of trans-  
95 formation strains fell considerably short of theoretical  
96 values by a factor of two to three in most cases. Most  
97 experiments on NiTiHf were conducted under compres-  
98 sion, while it is known that the NiTi-based alloys exhibit  
99 higher strains in tension [34]. Therefore, we focus attention  
100 on tensile transformation strain cases in this paper to shed  
101 light into the difference between transformation strains  
102 from theory and experiment.

103 Based on previous works, valuable insight has been  
104 gained through many articles and reviews on the SMA  
105 metrics of the NiTiHf alloys [18]. More recently, the digital  
106 image correlation (DIC) technique is used which is an

optical method of precise strain measurement by tracking 107  
the speckle patterns on specimen surfaces. The detailed 108  
procedures have been published elsewhere [35, 36]. The 109  
DIC provides insight into the spatial nature of the trans- 110  
formation strains, and can pinpoint active martensite 111  
regions and untransformed (elastic) domains. With DIC, 112  
high transformation strain exceeding 10% were measured 113  
in our previous work [37, 38] close to theory. In this work, 114  
large collections of new experimental results (different heat 115  
treatments, tension/compression, and compositions) are 116  
summarized in master plots on the transformation strains as 117  
a function of crystal orientations. Examples of superelas- 118  
ticity and shape memory experiments under stress are also 119  
demonstrated outlining the potential of NiTiHf alloys in the 120  
result section. 121

122 **Overview of Previous Work and Background**  
123 **of SMAs**

124 In this work, we included the characterization of the new 125  
NiTiHf ternary alloys with three different chemical com- 126  
positions,  $\text{Ni}_{50.5}\text{Ti}_{36.2}\text{Hf}_{13.3}$ ,  $\text{Ni}_{51.2}\text{Ti}_{23.4}\text{Hf}_{25.4}$ , and  $\text{Ni}_{50.3}$ - 127  
 $\text{Ti}_{25}\text{Hf}_{24.7}$  (at.%). Because of better mechanical responses, 128  
the results of  $\text{Ni}_{50.5}\text{Ti}_{36.2}\text{Hf}_{13.3}$  and  $\text{Ni}_{50.3}\text{Ti}_{25}\text{Hf}_{24.7}$  were 129  
presented in the as-grown condition in “**Experimental**  
130 **Results on NiTi13Hf and NiTi25Hf**” section, while those 131  
of  $\text{Ni}_{51.2}\text{Ti}_{23.4}\text{Hf}_{25.4}$  alloys were shown in the aged condi- 132  
tion (550 °C for 11 h). For the  $\text{Ni}_{50.3}\text{Ti}_{25}\text{Hf}_{24.7}$  alloy, the 133  
transformation temperatures measured from differential 134  
scanning calorimetry (DSC) are as follows: austenite start 135  
temperature  $A_s = 251$  °C, the austenite finish temperature 136  
 $A_f = 422$  °C, the martensite start temperature 137  
 $M_s = 340$  °C, and the martensite finish temperature 138  
 $M_f = 214$  °C. After aging at 500 °C for 4 h, we found that 139  
the transformation temperatures are similar to those of the 140  
as-grown materials. The single crystal samples were cut 141  
from an ingot once the desired crystallographic directions 142  
are established. This was achieved by heating the samples 143  
to 500 °C to the fully austenitic state and conducting X-ray 144  
diffraction in the austenitic state on the single crystal 145  
ingots. For the  $\text{Ni}_{50.5}\text{Ti}_{36.2}\text{Hf}_{13.3}$  alloy, the transformation 146  
temperatures are much lower:  $M_s = -31.7$  °C, 147  
 $M_f = -69.4$  °C,  $A_s = -14.8$  °C, and  $A_f = 31.2$  °C. The 148  
X-ray diffraction was used to orient these ingots as well, 149  
and then specimens were cut at desired orientations. In 150  
addition, the characterization of the superelasticity and 151  
shape memory effect of  $\text{Ni}_{51.2}\text{Ti}_{23.4}\text{Hf}_{25.4}$  (at.%) has been 152  
investigated thoroughly in our previous studies [39], which 153  
will not be elaborated here. Based on our strain values 154  
procured for both 13Hf and 25Hf materials, a large data- 155  
base has been established to gain an insight into the com- 156  
parison between the theoretical and experimental strain 157  
levels.

158 **Outline of the Present Work**

159 To achieve a better understanding of these class of NiTiHf  
 160 alloys, we undertake a comprehensive study that calculates  
 161 the theoretical transformation strains in NiTiHf over a  
 162 broad range of Hf contents and compare the results with  
 163 our experiments on 13Hf and 25Hf contents. Previous  
 164 experiments over the last 10 years have reported strains far  
 165 less than 4% for the NiTiHf alloys, while the present work  
 166 provides strain magnitudes that exceed 10% which is much  
 167 closer to theoretical predictions. The previous experimental  
 168 results were mostly in compression, and in the present  
 169 study, we also focus on tension with much higher strains.  
 170 We report the results of nearly 60 experiments with single  
 171 crystals oriented in selected orientations. We found that  
 172 [111] orientation is superior in tension to produce high  
 173 transformation strains, while orientations near the [011]  
 174 pole are more favorable in compression. The present work  
 175 has focused on both superelasticity and shape memory  
 176 (thermal cycling) experiments. Previous work has focused  
 177 on temperatures less than 250 °C, while in this work, our  
 178 transformation temperatures are near 400 °C for the 25Hf  
 179 composition.

180 The paper is organized as follows. (i) Firstly, we report  
 181 the lattice constants determined via density functional  
 182 theory (DFT) for 6.25, 12.5, and 25Hf compositions. Those  
 183 of 15 and 20Hf materials from literatures have been  
 184 included in this paper as well. A trend has been noted  
 185 between monoclinic angles and Hf compositions. A compar-  
 186 ison was made between the DFT results and those  
 187 measured via TEM diffraction patterns for the 25Hf case.  
 188 In addition, the microstructures of the samples with 25Hf  
 189 have been characterized in this work as well. (ii) Secondly,  
 190 the habit plane systems have been established for 6.25,  
 191 12.5, and 25Hf compositions. Based on the determined  
 192 habit plane system, the theoretical calculation of the  
 193 transformation (recoverable) strain for correspondent  
 194 variant pair (CVP) formation and detwinned martensite for  
 195 single-crystal NiTiHf has been undertaken. The prediction  
 196 of the transformation strains using lattice deformation  
 197 theory (LDT) was performed as well in this study. The  
 198 similarity between the CVP + detwin strain and LDT  
 199 strain is noted. These calculations pinpoint that the phase  
 200 transformation favors more in [011] under compression and  
 201 [111] under tension due to higher strain values near these  
 202 poles. (iii) The superelastic response in [011] under com-  
 203 pression and strain–temperature results under constant  
 204 stress in tension for [111] orientation are presented for two  
 205 Hf contents (~12.5 and 25Hf). The comparison of trans-  
 206 formation strains from the experiments with LDT strain has  
 207 been made. The polycrystal experimental results are also  
 208 included for the two selected Hf contents and the theoret-  
 209 ical strains are predicted based on the CVP formation, the

grain orientations measured with EBSD and a microme-  
 mechanical analysis.

Overall, this work provides a timely contribution to the  
 understanding of the new NiTiHf SMAs with a wide range  
 of Hf compositions (as high as 25%) via comparisons  
 between theoretical and experimental results. The good  
 agreement between the two confers great potential in this  
 class of materials. This work also highlights the need of a  
 multifaceted approach, including (i) the DFT calculations,  
 (ii) the TEM micrograph for characterizing microstruc-  
 tures, and (iii) the DIC measurement for pinpointing the  
 spatial distribution of the strain contours, for the future  
 SMA research.

**Results of the Present Work****Determination of Lattice Constants**

We consider alloys that follow the atomic composition  
 NiTi<sub>50-x</sub>Hf<sub>x</sub> with the Hf atomic content percentage  
 $x$  ranging from 0 to 25 for DFT calculations. The six dif-  
 ferent alloys considered in this work and their lattice  
 constants are plotted (Fig. 1). For the cubic to monoclinic  
 transformation strain determination, the lattice constants  
 include the cubic (B2) constant  $a_0$  and monoclinic (B19')  
 constants  $a$ ,  $b$ ,  $c$ , and the monoclinic angle. For the

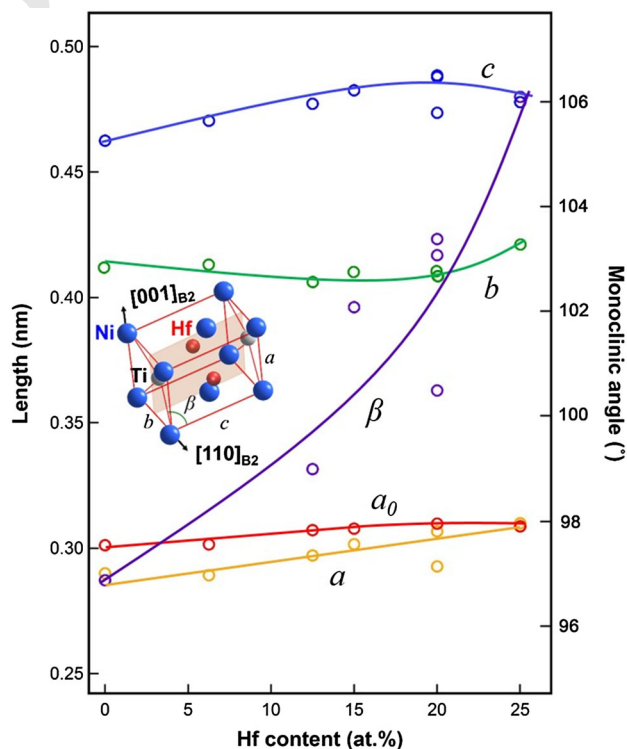


**Fig. 1** The variation of the lattice parameters and the monoclinic angle with increasing Hf content. The lines are drawn to aid the eye

233 monoclinic crystal structures,  $c$  is the longest axis,  $a$  is the  
234 shortest axis, and  $b$  is intermediate in length. The mono-  
235 clinic angle ( $\beta$ ) is the angle between the  $a$  and  $c$  axes. For  
236 an orthorhombic structure, the monoclinic angle would be  
237  $90^\circ$ . For the B19' crystal, it increases from  $97^\circ$  to  $106^\circ$  with  
238 increasing Hf, which is substantial.

239 The lattice constants in Fig. 1 for the 0%Hf, 15%Hf, and  
240 20%Hf are obtained from experiments summarized in  
241 Table 1. The corresponding chemical compositions and  
242 principal investigators have been included as well. The  
243 designations HS, DH, HK, OB, and AS refer to Sehitoglu,  
244 Hodgson, Karaca, Benafan, and Stebner's work, respec-  
245 tively. For the 6.25, 12.5, and 25Hf cases, the lattice con-  
246 stants are obtained from DFT calculations ([16], Appendix  
247 1), and we also confirmed the 25Hf lattice constants from  
248 the electron diffraction experiments in this study. The  
249 values of the experimental lattice constants have shown to  
250 differ depending on the investigator (for the 15 and 20Hf  
251 cases) but the increasing monoclinic angle with increasing  
252 Hf content is a common trend. Cubic (B2) to monoclinic  
253 (B19') martensitic phase transformation occurs for alloys  
254 with Hf content in the range from 6.25 to 25%. The  
255 energies of the orthorhombic (B19) and B19' phases are  
256 included as references (Appendix 1) showing the lower  
257 energy for the B19' lattice structure. The small energy  
258 difference between the two phases is noted, so these results  
259 do not preclude the possibility of B19 domains for the 25Hf  
260 case, but it is expected that B19' structure is dominant.

## 261 Transformation Strains for CVP Formation

262 During the phase transformation from austenite to  
263 martensite, the newly formed martensite crystal is inter-  
264 nally twinned. The two twin-related martensite variants are  
265 called a correspondent variant pair, or CVP. As the phase  
266 transformation progresses, the twinned martensite crystal  
267 begins to experience detwinning, a process in which one  
268 variant within the CVP grows at the expense of the other  
269 [21]. We compute two values of transformation

(recoverable) strains for single crystals. The transformation  
270 strain from the formation of CVPs is called the CVP for-  
271 mation strain, or simply the CVP strain. The transformation  
272 strain from the formation and detwinning of CVPs is called  
273 the CVP formation and detwinning strain, or simply the  
274 CVP detwinning strain ( $\varepsilon_{\text{CVP} + \text{detwin}}$ ). Since  $\varepsilon_{\text{CVP} + \text{detwin}}$   
275 includes both CVP formation and detwinning, it is an  
276 estimate of the total transformation strain. Another way to  
277 model the total transformation strain for single crystals is  
278 the lattice deformation theory (LDT) [43]. The LDT cal-  
279 culates the upper limit of the recoverable strain by  
280 assuming that austenite transforms into single crystal of  
281 martensite. Both the LDT strain  $\varepsilon_{\text{LDT}}$  and  $\varepsilon_{\text{CVP} + \text{detwin}}$  are  
282 calculations of the total transformation strain, and as  
283 expected, we show that a close correspondence exists  
284 between the two. LDT strains for [111] tension as a func-  
285 tion of Hf content are shown in Fig. 2.

287 For NiTi and NiTiHf alloys, a number of different  
288 twinning modes may coexist in the martensite crystal  
289 during the phase transformation (Table 2). These modes of  
290 twinning are classified by their twin plane (interface plane  
291 between the variants in a CVP) normal  $\mathbf{n}$  and twinning  
292 shear direction  $\mathbf{a}$ . In Type I twins, the twin plane normal  
293 has rational indices. In Type II twins, the twin shear  
294 direction has rational indices. In compound twins, both the  
295 twin plane normal and twin shear direction have rational  
296 indices. Although the [011]-Type II is the predominant  
297 twinning mode in the binary NiTi alloy [22], the most  
298 frequently observed twinning modes for NiTiHf alloys with  
299 high Hf content are the (011)-Type I and (001) [001]-  
300 Compound twins [32]. Therefore, the energy minimization  
301 calculations are focused on the (011)-Type I and (001)  
302 [001]-Compound twins for all alloys considered in this  
303 work. Two habit plane solutions are obtained as shown in  
304 Table 2 where the  $\mathbf{m}$  and  $\mathbf{b}$  designate the habit plane nor-  
305 mal and habit plane shear, respectively. In the next sec-  
306 tions, we explain the determination of the  $\mathbf{a}$ ,  $\mathbf{n}$ ,  $\mathbf{b}$ , and  
307  $\mathbf{m}$  and the computation of the CVP strain formation fol-  
308 lowed by lattice deformation calculations.

**Table 1** A summary of the chemical compositions of the alloys from literature and current work

Material designation	Chemical composition (at.%)	Principal investigator
NiTi	Ni <sub>50</sub> Ti <sub>50</sub>	[40]; HS [16]
NiTi6.25Hf	Ni <sub>50</sub> Ti <sub>43.75</sub> Hf <sub>6.25</sub>	HS [16]
NiTi12.5Hf	Ni <sub>50</sub> Ti <sub>37.5</sub> Hf <sub>12.5</sub>	HS [16]
NiTi13Hf	Ni <sub>50.5</sub> Ti <sub>36.2</sub> Hf <sub>13.3</sub>	This study
NiTi15Hf	Ni <sub>49.8</sub> Ti <sub>35.2</sub> Hf <sub>15</sub>	DH [9]
NiTi20Hf	Ni <sub>50.3</sub> Ti <sub>29.7</sub> Hf <sub>20</sub>	HK [41]; AS [19]; OB [42]
	Ni <sub>49.8</sub> Ti <sub>30.2</sub> Hf <sub>20</sub>	DH [9]
NiTi25Hf	Ni <sub>50</sub> Ti <sub>25</sub> Hf <sub>25</sub>	HS [16]
	Ni <sub>51.2</sub> Ti <sub>23.4</sub> Hf <sub>25.4</sub>	This study
	Ni <sub>50.3</sub> Ti <sub>25</sub> Hf <sub>24.7</sub>	

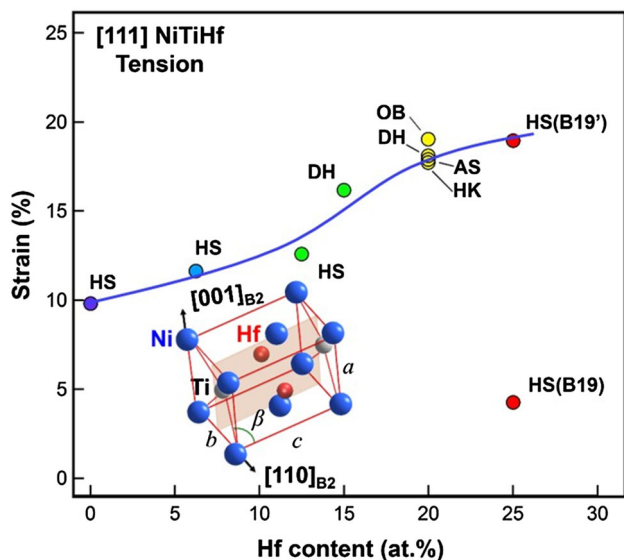


**Fig. 2** The LDT strain for [111] single crystal under tension. The inset shows the monoclinic lattice. The lattice constants obtained from different investigators are marked with their initials

**CVP Formation and CVP Detwinning Strain**

309

The lattice orientations of the parent and twin phases are related through a number of different lattice correspondence variants. There are a total of 12 lattice correspondence variants for a cubic to monoclinic transformation, and six variants for a cubic to orthorhombic transformation. For each lattice correspondence variant, a deformation gradient tensor  $\mathbf{F}$  and its symmetric part  $\mathbf{U}$  can be determined. The components of the  $\mathbf{F}$  and  $\mathbf{U}$  matrices are functions of the lattice constants [22]. The lattice constants used in the calculations have been summarized earlier in Fig. 1. There are some differences in the constants for NiTi20Hf among DH, HK, OB, and AS, but the transformation strains calculated are rather close.

The kinematic compatibility between the two variants in the CVP across the twin plane requires that

$$\mathbf{R}_{ij}\mathbf{U}_j - \mathbf{U}_i = \mathbf{a} \otimes \mathbf{n} \tag{1}$$

where  $\mathbf{U}_i$  and  $\mathbf{U}_j$  represent the  $i$ -th and  $j$ -th variants forming the CVP,  $\mathbf{R}_{ij}$  is an orthogonal rotation tensor between the two variants,  $\mathbf{n}$  is the twinning plane normal, and  $\mathbf{a}$  is the

**Table 2** Twinning modes used in energy minimization calculations

Material (investigator)	Twinning mode	Twin plane normal ( $n$ )	Twin shear direction ( $a$ )	Habit plane normal ( $m$ )	Habit shear direction ( $b$ )
NiTi6.25Hf (HS)	(011)-Type I	{0.7071 0.7071 0}	<0.0909 0.1382 0.3323>	{-0.2675 0.8514 -0.4512}	<0.1111 -0.0078 -0.0662>
				{-0.8412 0.0048 0.5408}	<0.0417 -0.1103 0.0539>
NiTi12.5Hf (HS)	(011)-Type I	{0.7071 0.7071 0}	<0.0457 0.1015 0.3874>	{-0.2339 0.9335 -0.2718}	<0.1029 -0.0181 -0.0667>
				{-0.8236 0.0888 0.5602}	<0.0350 -0.1153 0.0291>
NiTi15Hf (DH)	(011)-Type I	{0.7071 0.7071 0}	<0.0341 0.1066 0.4495>	{-0.1058 0.9093 -0.4025}	<0.1511 -0.0115 -0.0632>
				{-0.9090 -0.0045 0.4169}	<0.0297 -0.1497 0.0607>
NiTi20Hf (HK)	(011)-Type I	{0.7071 0.7071 0}	<0.0161 0.1018 0.4947>	{-0.0666 0.9111 -0.4067}	<0.1677 -0.0118 -0.0651>
				{-0.9184 -0.0168 0.3952}	<0.0270 -0.1651 0.0674>
NiTi25Hf (HS)	(011)-Type I	{0.7071 0.7071 0}	<0.0197 0.0982 0.4744>	{-0.0125 0.8204 -0.5716}	<0.2338 -0.0060 -0.0390>
				{-0.9708 -0.0709 0.2292}	<0.0303 -0.1953 0.1310>
NiTi25Hf (HS)	(001) [001] Compound	{1 0 0}	<0.0123 0.2237 0>	{-0.6348 0.5926 -0.4958}	<0.0357 0.0316 -0.0264>

329 twinning shear direction. There is no summation of the  
330 index.

331 The kinematic compatibility between the twinned  
332 martensite and parent austenite requires that

$$\mathbf{F}_M - \mathbf{I} = \mathbf{b} \otimes \mathbf{m} \quad (2)$$

334 where  $\mathbf{I}$  is the identity tensor,  $\mathbf{m}$  is the habit plane (interface  
335 plane between the twinned martensite and parent phase)  
336 normal, and  $\mathbf{b}$  is the martensitic transformation shear. For a  
337 stack of thin twin layers,  $\mathbf{F}_M$  is defined by

$$\mathbf{F}_M = \mathbf{R}_h (f \mathbf{R}_{ij} \mathbf{U}_j + (1-f) \mathbf{U}_i) \quad (3)$$

339 where  $f$  and  $1-f$  are the volume fractions of the two lattice  
340 correspondence variants, and  $\mathbf{R}_h$  is the relative rotation  
341 between the twinned martensite and the parent phase.

342 Substituting Eqs. (1) and (3) into Eq. (2),

$$\mathbf{R}_h (\mathbf{U}_i + f \mathbf{a} \otimes \mathbf{n}) = \mathbf{I} + \mathbf{b} \otimes \mathbf{m} \quad (4)$$

344 There are 84 equations in Eq. (4), which means that there  
345 are 84 sets of  $(\mathbf{a}, \mathbf{n})$  in theory. However, some sets of lattice  
346 constants may not have all 84 solutions.

347 A symmetric matrix  $\mathbf{C}$  is defined as

$$\mathbf{C} = \mathbf{F}_M^T \mathbf{F}_M \quad (5)$$

349 Substituting for  $\mathbf{F}_M$  in terms of  $f$ , the matrix  $\mathbf{C}(f)$  can be  
350 rewritten as

$$\mathbf{C}(f) = (\mathbf{U}_i + f \mathbf{n} \otimes \mathbf{a})(\mathbf{U}_i + f \mathbf{a} \otimes \mathbf{n}) \quad (6)$$

352 In order for Eq. (4) to have solutions,  $\mathbf{C}(f)$  must have  
353 ordered eigenvalues of  $\lambda_1 \leq \lambda_2 = 1 \leq \lambda_3$ , which can be  
354 obtained from

$$\det(\mathbf{C}(f) - \mathbf{I}) = 0 \quad (7)$$

356 Using the ordered eigenvalues  $\lambda_1 \leq \lambda_2 = 1 \leq \lambda_3$ , the  
357 solutions of  $\mathbf{b}$  and  $\mathbf{m}$  are

$$\mathbf{b} = \rho \left( \sqrt{\frac{\lambda_3(\lambda_2 - \lambda_1)}{\lambda_3 - \lambda_1}} \mathbf{e}_1 - \kappa \sqrt{\frac{\lambda_1(\lambda_3 - \lambda_2)}{\lambda_3 - \lambda_1}} \mathbf{e}_3 \right) \quad (8)$$

$$\mathbf{m} = \rho^{-1} \left( \frac{\sqrt{\lambda_3} - \sqrt{\lambda_1}}{\sqrt{\lambda_3} - \lambda_1} \right) \left( -\sqrt{\lambda_2 - \lambda_1} \mathbf{e}_1 + \kappa \sqrt{\lambda_3 - \lambda_2} \mathbf{e}_3 \right), \quad (9)$$

361 where  $\rho$  is a constant used to normalize the vectors and  
362  $\kappa = \pm 1$ , which means Eqs. (8) and (9) represent two sets  
363 of  $(\mathbf{b}, \mathbf{m})$ . In theory, there are a total of 192 sets of  $(\mathbf{b}, \mathbf{m})$ ,  
364 after taking solutions for both  $f$  and  $1-f$  into account.  
365 However, some sets of lattice constants may not have all  
366 192 solutions for  $(\mathbf{b}, \mathbf{m})$ .

367 After having determined the sets of  $(\mathbf{b}, \mathbf{m})$ , the trans-  
368 formation CVP strain,  $\varepsilon_{\text{CVP}}$ , can be calculated as

$$\varepsilon = \frac{1}{2} (\mathbf{F}_M^T \mathbf{F}_M - \mathbf{I}) \quad (10)$$

$$= \frac{1}{2} (\mathbf{b} \otimes \mathbf{m} + \mathbf{m} \otimes \mathbf{b} + (\mathbf{b} \cdot \mathbf{b}) \mathbf{m} \otimes \mathbf{m}) \quad (11) \quad 370$$

To calculate the detwinning strain, the volume fraction  $f$  is  
372 set to 0 if  $f < 0.5$ . This changes the  $\mathbf{F}_M$  matrix from Eq. (3)  
373 to  
374

$$\mathbf{F}_M^{\text{dt}} = \mathbf{R}_h \mathbf{U}_i \quad (12)$$

If  $f > 0.5$ , then  $f$  is set to 1. In this case, the  $\mathbf{F}_M^{\text{dt}}$  matrix is  
376

$$\mathbf{F}_M^{\text{dt}} = \mathbf{R}_h \mathbf{R}_{ij} \mathbf{U}_j = \mathbf{R}_h \cdot (\mathbf{U}_i + \mathbf{a} \otimes \mathbf{n}) \quad (13)$$

Using  $\mathbf{F}_M^{\text{dt}}$ , the total transformation strain (CVP formation  
378 and detwinning),  $\varepsilon_{\text{CVP} + \text{detwin}}$ , can be calculated in a  
379 similar way as Eq. (10), with  $\mathbf{F}_M$  being replaced by  $\mathbf{F}_M^{\text{dt}}$ .  
380

### Lattice Deformation Theory Calculations 381

The total transformation strain for single crystals can also  
382 be calculated using LDT. Unlike the energy minimization  
383 theory, LDT assumes that a single crystal of austenite  
384 transforms into a single crystal of martensite, without  
385 considering the effect of twinning. Therefore the total  
386 transformation strain is directly calculated using the  
387 deformation gradient tensor  $\mathbf{F}$  [43, 44],  
388

$$\varepsilon_{\text{LDT}} = \sqrt{\hat{\mathbf{e}} \cdot (\mathbf{F}^T \mathbf{F} \hat{\mathbf{e}})} - 1 \quad (14)$$

where  $\mathbf{F}$  is the deformation gradient tensor for a lattice cor-  
390 respondence and  $\hat{\mathbf{e}}$  is the unit vector in the direction of the  
391 single crystal's orientation. There are 12 such correspon-  
392 dences in the cubic to monoclinic transformation, and all 12  
393 are utilized to select the one that renders the highest strain.  
394

Both  $\varepsilon_{\text{LDT}}$  and  $\varepsilon_{\text{CVP} + \text{detwin}}$  calculations yield essen-  
395 tially the same transformation strain values. LDT does not  
396 consider the intermediate processes of CVP formation, and  
397 considers transition from single crystal of pristine austenite  
398 to single crystal of martensite. Clearly, the calculations  
399 represent an ideal case because the presence of precipitates  
400 and slip domains at interfaces will result in a deviation  
401 from the ideal conditions.  
402

The NiTiHf alloys with different Hf content are distin-  
403 guished from one other in the transformation strain calcu-  
404 lations by variations in lattice parameters. The lattice  
405 parameter that shows the most noticeable variation is the  
406 monoclinic angle, which displays a clear positive correla-  
407 tion with Hf content (Fig. 1). The LDT calculations are  
408 given in Figs. 3 and 4. The two most important orientations  
409 of interest are the [111] and [011] ones. The results show  
410 that with increasing Hf content, the transformation strains  
411 to rather high levels in tension and increase to moderately  
412 high levels in compression (Figs. 3, 4).  
413

The transformation strains with increasing Hf content  
414 are given in the stereographic triangles in Figs. 4, 5, 6, and  
415

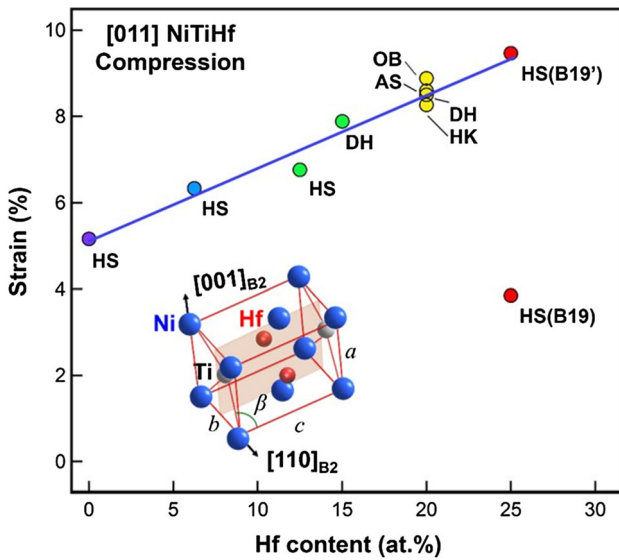
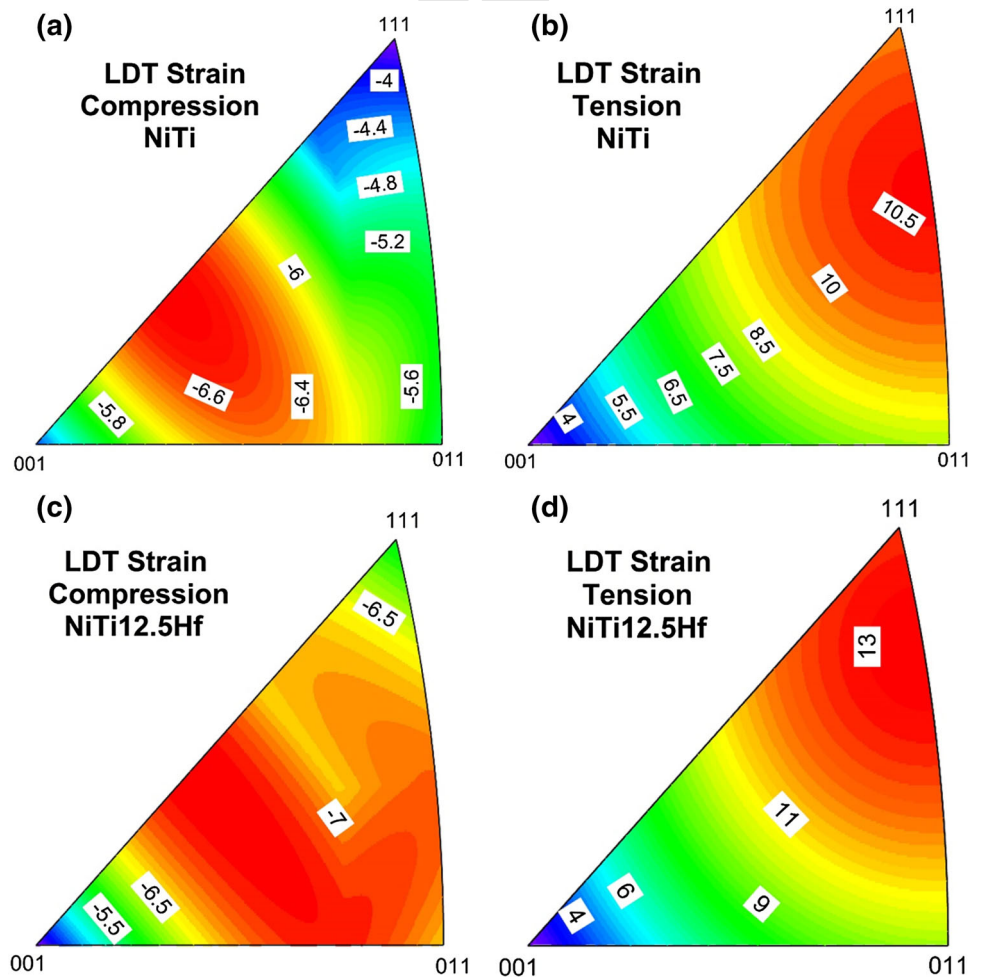


**Fig. 3** The LDT strain for [011] single crystal under compression, the inset shows the monoclinic lattice for 25Hf composition. The lattice constants obtained from different investigators are marked with their initials

**Fig. 4** The LDT strain contours for single crystals of NiTi and NiTi12.5Hf (cubic to monoclinic). We note the increase in transformation strains with addition of Hf



7. The maximum compressive  $\epsilon_{LDT}$  increases to 11.5% for NiTi25Hf (for the [112] orientation). The maximum tensile  $\epsilon_{LDT}$  increases from 10.7% for NiTi (for the [774] orientation) to 19% for NiTi25Hf (for the [111] orientation).

For single crystals with [001] orientation, the compressive  $\epsilon_{LDT}$  decreases with increasing Hf content. As the Hf content is increased, the crystal orientation of the maximum compressive  $\epsilon_{LDT}$  experiences a shift towards [112], which is closer to [011] than [001]. Therefore, the [001] pole experiences a decrease in compressive  $\epsilon_{LDT}$  at higher Hf contents, while the [011] orientation experiences an increase in compressive  $\epsilon_{LDT}$  at higher Hf contents. A similar pattern of a shift in the crystal orientation of the maximum strain is also present for the tensile  $\epsilon_{LDT}$ . For tensile  $\epsilon_{LDT}$ , the orientation of the maximum strain shifts from the [774] orientation for NiTi towards the [111] orientation for NiTiHf alloys with high Hf content (Table 3; Fig. 7). These shifts in the crystal orientation of the high transformation strains are ultimately caused by the changes in the lattice constants induced by the increase in Hf

**Fig. 5** The LDT strain contours for NiTi25Hf single crystals (cubic to monoclinic)

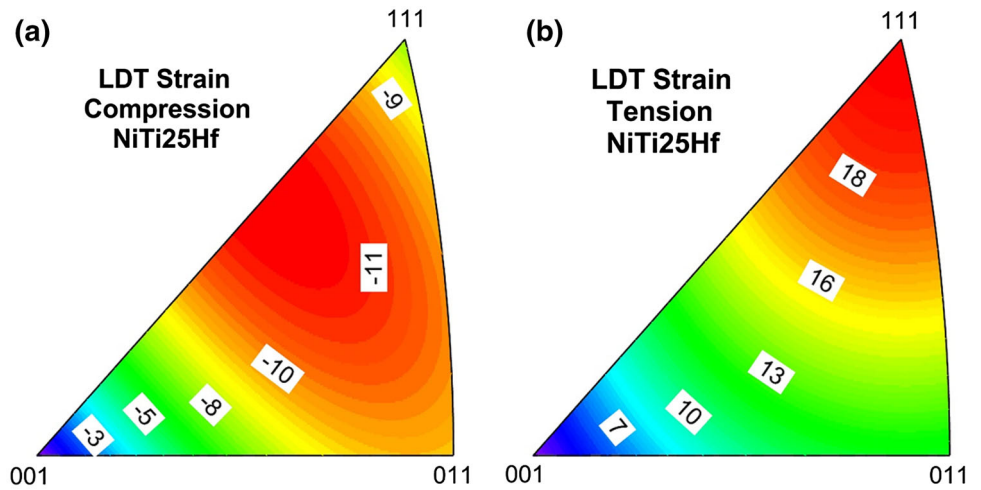
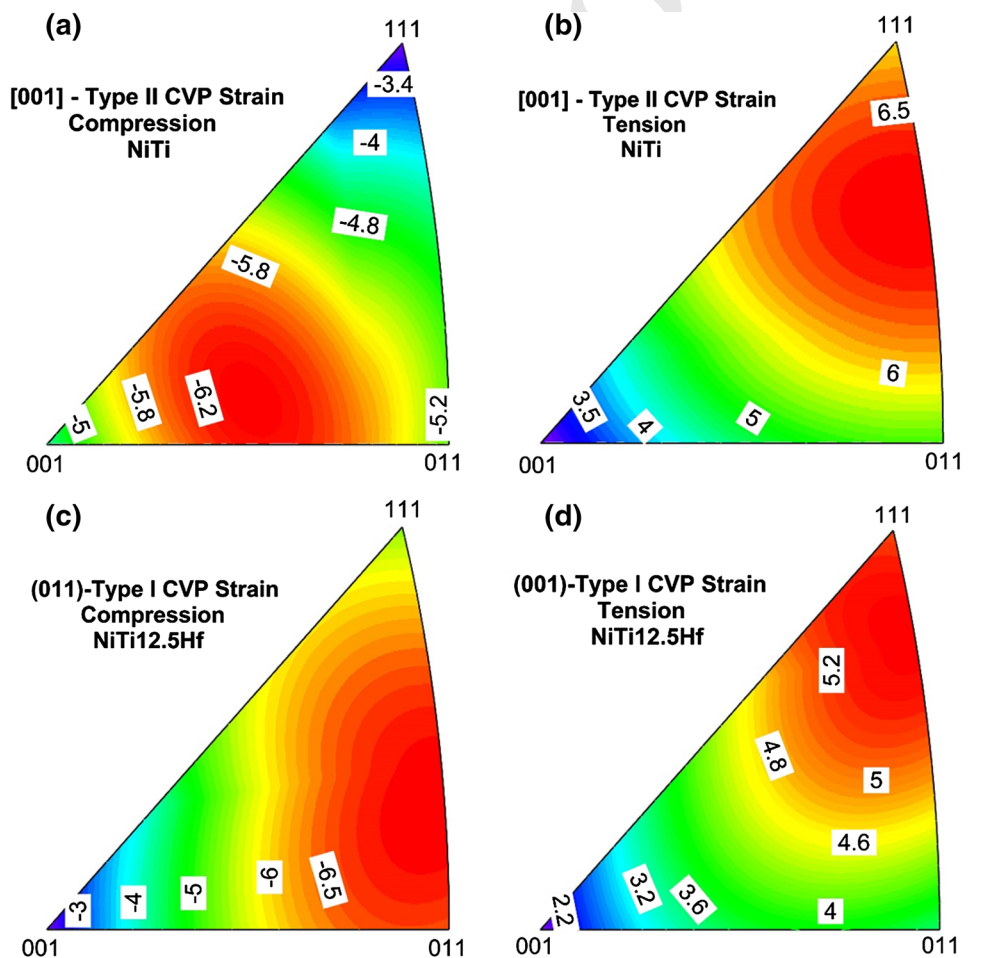


**Fig. 6** [001]-Type II CVP strain contours for single-crystal NiTi; (011)-Type I CVP strain contours for single-crystal NiTi12.5Hf (cubic to monoclinic) for compression and tension. We note that the CVP formation strain is much lower than LDT strain in tension



436 content, and most prominently the increase in the mono-  
 437 clinic angle.  
 438 The (011)-Type I twinning is of particular interest in this  
 439 work, because it is generally the predominant mode of  
 440 twinning in NiTiHf alloys [32]. Under compressive load-  
 441 ing, the difference between (011)-Type I  $\epsilon_{CVP}$  and

$\epsilon_{CVP} + \detwin$  is very small. Under tensile loading, the dif-  
 442 ference is large (often  $>40\%$ ) for the (011)-Type I case.  
 443 Overall, the model therefore predicts that the detwinning  
 444 strain is much more significant for deformation under  
 445 tension than under compression.  
 446

**Fig. 7** (011)-Type I CVP strain contours for single crystals of NiTi25Hf (cubic to monoclinic). The tension compression asymmetry of the transformation strains is noted

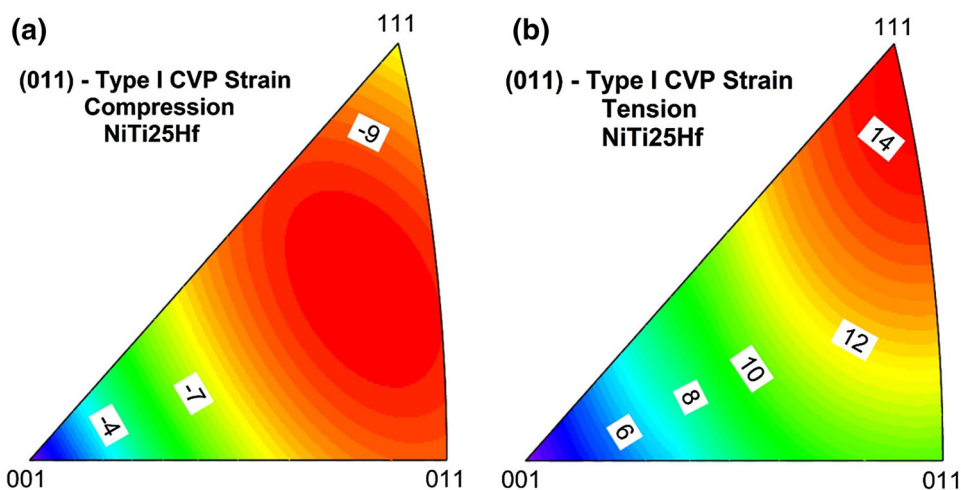


**Table 3** Theoretical compressive transformation strains based on cubic to monoclinic model

	[111] Single crystal			[011] Single crystal			[001] Single crystal		
	(011)-Type I CVP strain (%)	(011)-Type I CVP and detwinning strain (%)	LDT strain (%)	(011)-Type I CVP strain (%)	(011)-Type I CVP and detwinning strain (%)	LDT Strain (%)	(011)-Type I CVP strain (%)	(011)-Type I CVP and detwinning strain (%)	LDT strain (%)
NiTi* (HS) Type II-1	2.98	3.58	3.64	5.06	5.04	5.17	4.37	4.09	4.18
NiTi6.25Hf (HS)	3.99	3.99	4.08	6.13	6.13	6.33	2.91	4.63	4.75
NiTi12.5Hf (HS)	5.40	5.40	5.55	6.54	6.54	6.77	2.37	2.37	3.41
NiTi15Hf (DH)	4.44	4.44	4.55	7.56	7.56	7.87	1.58	1.93	1.95
NiTi20Hf (HK)	4.48	4.48	4.58	8.00	8.00	8.35	1.11	1.11	0.97
NiTi20Hf (OB)	4.93	4.93	5.05	8.50	8.50	8.89	1.34	1.45	1.46
NiTi20Hf (DH)	4.04	4.04	4.90	7.93	7.93	8.28	1.18	1.18	0.97
NiTi20Hf (AS)	4.70	4.70	4.82	8.17	8.17	8.53	1.36	1.36	1.29
NiTi25Hf (HS)	7.55	7.55	7.86	9.01	9.01	9.46	0.291	0	0

Note that orientations near [011] pole produce strains as high as 9.5% in compression for NiTi25Hf

\* CVP strain and CVP detwinning strain for NiTi are for [001]-Type II twin

447 **Determination of Twinning Mode with TEM**

448 Figure 8 shows typical selected area electron diffraction  
 449 pattern (SAEDP) taken from NiTi25Hf aged at 500 °C for  
 450 4 h along [110]<sub>B19'</sub>, which corresponds to <111><sub>B2</sub>. There  
 451 are nine sets of reflections, i.e., 3 (001)<sub>B19'</sub> compound twin-  
 452 related martensites, and three precipitate variants. They can

be consistently indexed by lattice parameters of monoclinic  
 martensite:  $a = 0.309$ ,  $b = 0.421$ ,  $c = 0.478$  nm, and  
 $\beta = 105.9^\circ$ , and orthorhombic precipitate (H-phase):  
 $a = 1.264$ ,  $b = 0.882$ , and  $c = 2.608$  nm, respectively.

Morphological and crystallographic aspects of marten-  
 sitic and precipitate phases are presented in Fig. 9. Fig-  
 ure 9(a, b) shows the bright-field (BF) image and

460 corresponding SAEDP, respectively. The details of SAEDP  
 461 have been discussed in Fig. 8. There are fine striations less  
 462 than 5 nm and particles about 10 nm in diameter with dark  
 463 contrast in (a). The striations are clearly visualized in each  
 464 of dark-field images in Fig. 9(c–e) taken using DF1–3  
 465 reflections in (b), respectively. The SAEDP and dark-field  
 466 (DF) images suggest that there are 3 habit plane variants  
 467 M1–M3 consisting of  $(001)_{B19'}$  compound twins in the

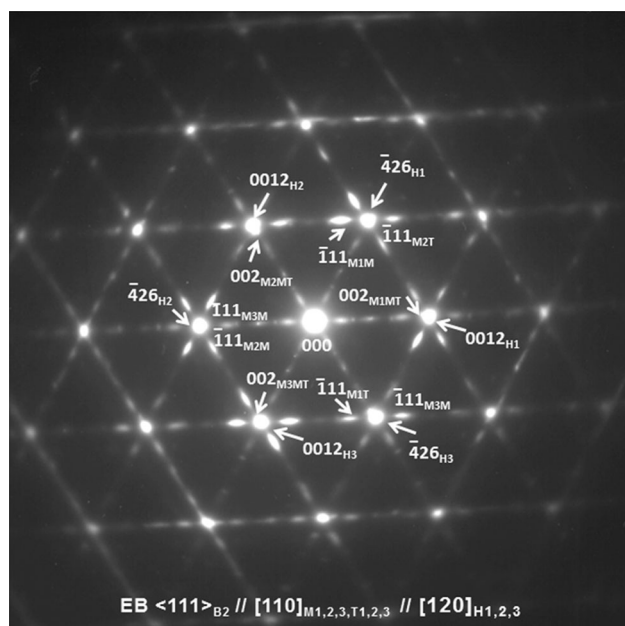
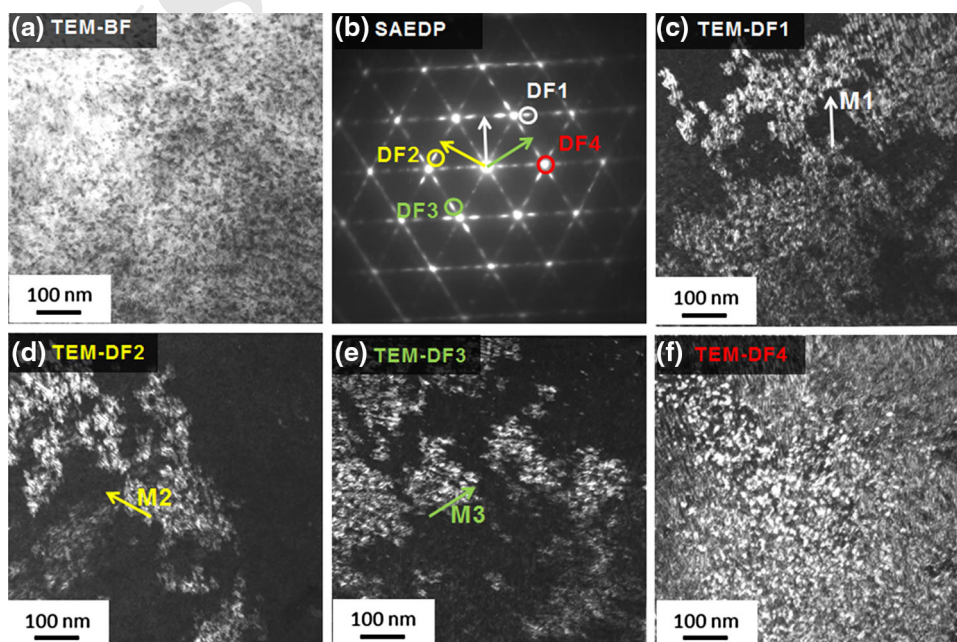


**Fig. 8** Typical SAEDP taken from NiTi25Hf aged at 500 °C for 4 h along  $[110]_{B19'}$ . The lattice constants obtained match the DFT calculations.  $a = 0.309$ ,  $b = 0.421$ ,  $c = 0.478$  nm, and  $\beta = 105.9^\circ$  (see Appendix 1)

**Fig. 9** **a** BF image and **b** corresponding SAEDP taken from NiTi25Hf aged at 500 °C for 4 h. **c–f** DF images taken using DF1–4 reflections, respectively



468 observed area. The twinning mode of the martensite is  
 469 again discussed later. The interface between habit plane  
 470 variants is very complicated in comparison to that in the  
 471 solution-treated NiTi binary system [45]. The similar  
 472 martensite morphology has been observed in aged Ni-rich  
 473 NiTi binary alloy including fine  $Ni_4Ti_3$  precipitates [46].  
 474 The size of precipitate, i.e., H-phase, is about 10 nm as  
 475 mentioned above. It is noteworthy from the DF image in  
 476 Fig. 9(f) that the H-phase in NiTi25Hf has block shape  
 477 rather than lenticular one in low Hf content alloys [28, 39].

478 Figure 10 shows SAEDP taken from NiTi25Hf aged at  
 479 500 °C for 4 h along  $[100]_{B19'}$ , which is parallel to  
 480  $\langle 100 \rangle_{B2}$ . The pattern consists of eight sets of reflections,  
 481 i.e., 2  $(011)_{B19'}$ -Type I twin-related martensites and four  
 482 precipitate variants. They can be also consistently indexed  
 483 by lattice parameters of monoclinic martensite and  
 484 orthorhombic precipitate, respectively.

485 Figure 11(a, b) shows the bright-field (BF) image and  
 486 corresponding SAEDP, respectively. The details of SAEDP  
 487 are discussed in Fig. 10. There are alternated platelets  
 488 about 10 nm or less in width and particles about 10 nm in  
 489 diameter with dark contrast in (a). The platelets are clearly  
 490 visualized in each of dark-field images in Fig. 11(c–e)  
 491 taken using DF1–3 reflections in (b), respectively. The  
 492 SAEDP and dark-field images suggest that there are two  
 493 habit plane variants M1 and M2 consisting of  $(011)_{B19'}$   
 494 Type I twins in the observed area. DF image in Fig. 11(f)  
 495 is out of BF image where the Bragg condition is slightly not  
 496 satisfied. However, precipitates are clearly visible. The  
 497 shape and size of precipitate are similar to those in Fig. 9,  
 498 although the incident electron beam is different. This also  
 499 suggests that the shape of precipitate is blocky rather than

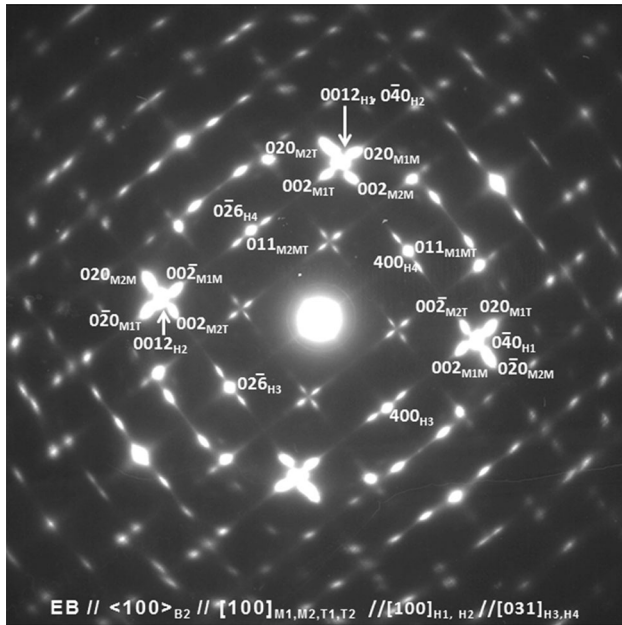
500 lenticular. From these observations, it is concluded that  
 501 there are  $(001)_{B19'}$  compound twins in  $(011)$  Type I twin  
 502 plates. The same situation has been observed in  
 503 NiTi2.5Hf alloy [28]. We have further illustration of the  
 504 presence of  $(011)$  Type I twin plates and  $(001)_{B19'}$   
 505 compound twins in the solutionized case in Fig. 12(a–d)  
 506 because the calculations for the transformation strains  
 507 assume solutionized conditions. Therefore, it is important  
 508 to confirm that there is no change between the aged and

509 solutionized case in terms of the twin system. Figures 12  
 510 and 13 show the existence of  $(011)$  Type I and  $(001)$   
 511 compound twins, respectively. The corresponding electron  
 512 diffraction patterns can be consistently indexed by lattice  
 513 parameters of monoclinic martensite:  $a = 0.309$ ,  
 514  $b = 0.421$ ,  $c = 0.478$  nm, and  $\beta = 105.9^\circ$ .

**Experimental Results on NiTi13Hf and NiTi25Hf**

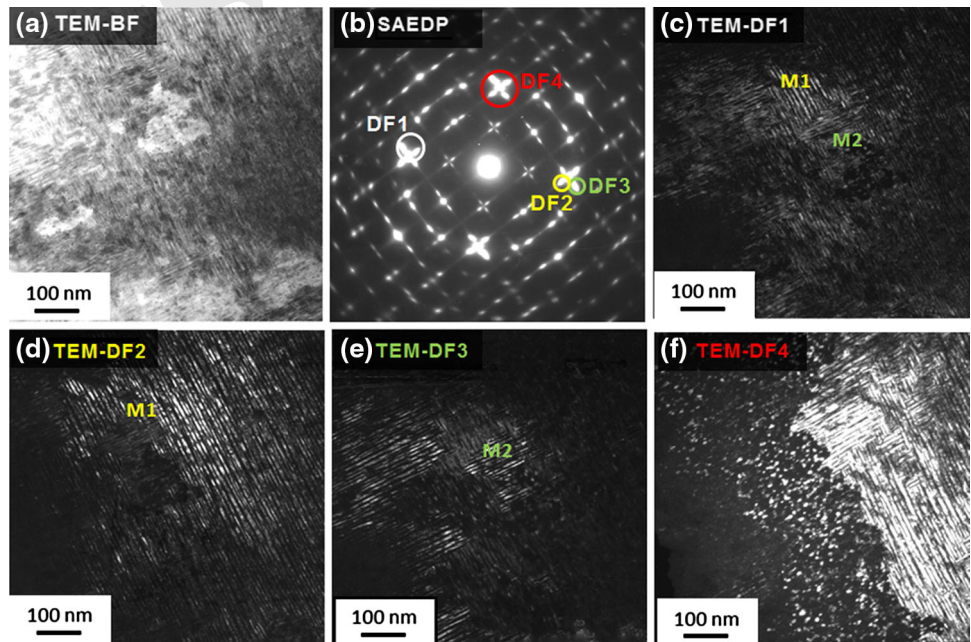
515  
 516 We provide a summary of our experimental results for the  
 517 13Hf and 25Hf cases that have not been published in our  
 518 previous studies in Figs. 14, 15, 16, and 17. In Fig. 14,  
 519 the results show the superelasticity of the 13Hf alloy exhibiting  
 520 strains exceeding 6.5% for  $[111]$  orientation in compression.  
 521 The DIC images are depicted at locations 1 and 2 of the  
 522 stress–strain curve. The strains are fully recovered upon  
 523 unloading. The DIC results can be used to define a local  
 524 and global strain measure. As noted in the insets in Fig. 14,  
 525 there are elastic domains that do not transform. The local  
 526 measure of strain represents the intrinsic transformation  
 527 strain without the influence of the elastic domains. Such  
 528 high strains in compression exceed previously reported  
 529 values. We note that the stress magnitudes are as high as  
 530 1500 MPa which can open new application for this alloy.

531 In Fig. 15, the results are shown for isobaric experi-  
 532 ments for the 13Hf for  $[111]$  orientation in tension. The  
 533 temperature is cycled under constant stress. The strain  
 534 levels exceeded 13% in tension which are higher than  
 535 previously reported experimental levels in binary NiTi  
 536 [21, 47]. As stated earlier, small increases in Hf can result  
 537 in considerable elevation of the transformation strain.



**Fig. 10** SAEDP taken from NiTi25Hf aged at 500 °C for 4 h along  $[100]_{B19'}$

**Fig. 11** a BF image and b corresponding SAEDP taken from NiTi25Hf aged at 500 °C for 4 h. c–f DF images taken using DF1–4 reflections, respectively



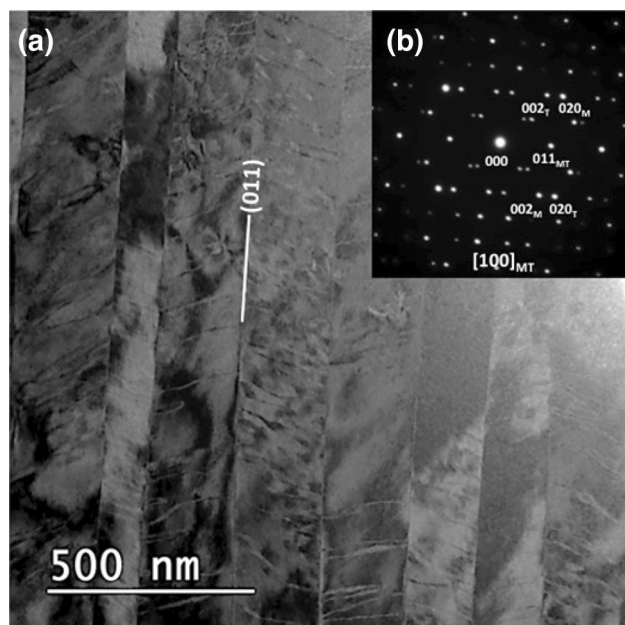


**Fig. 12** **a** The TEM image and **b** the corresponding SAEDP taken from a solutionized specimen showing the activation of the (011) Type I twin plates

538 In Fig. 16, the compressive superelastic response of the  
539 high Ni content NiTi25Hf single crystals orientated along  
540 [011] direction has been shown at 200 °C. The specimen  
541 was aged at 550 °C for 11 h. The transformation strain of  
542 the order of near 3% locally has been shown under the  
543 overaged condition.

544 The tensile experimental result for the low Ni content  
545 NiTi25Hf alloys is shown in Fig. 17 under temperature  
546 cycling. Both local and global strains are shown, and the  
547 transformation strain in tension is nearly 10%. The  
548 remarkable observation is that the  $A_f$  exceeds 400 °C. In  
549 Fig. 17(b), we compare the traces of the habit planes as  
550 evident from the strain localization with the variants pre-  
551 dicted from the phenomenological theory. The habit planes

**Fig. 13** **a** The TEM Image displaying the (011) Type I twin plates, and **b** the presence of compound (001) twins within the (011) Type I twin plates, and (c) corresponding SAEDP pattern

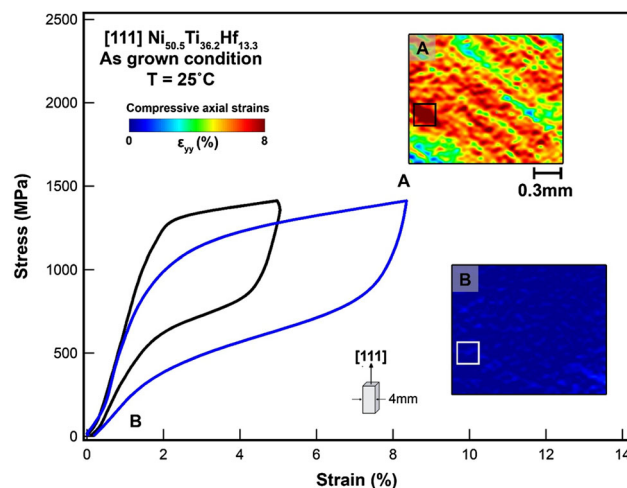
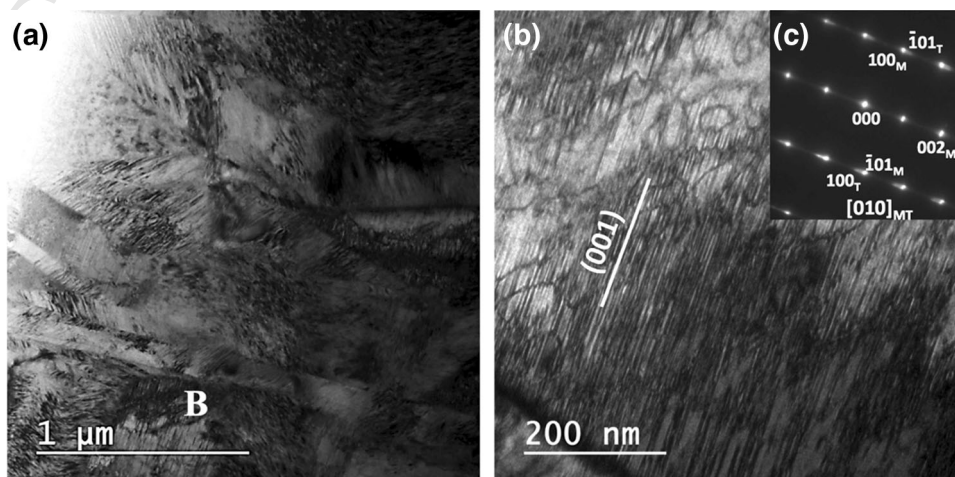


**Fig. 14** The stress–strain response of NiTi13Hf under compression ([111] orientation). The *dashed line* corresponds to average strain over a smaller area shown above

associated with variants #3, #11, and #9 coincide with the 552  
553 austenite/martensite interfaces that are noted in the DIC  
554 images below. The variants #3, #9, and #11 belong to the  
555 habit plane family given in Table 2 as  $\{-0.0125\ 0.8204$   
556  $-0.5716\}$ . Note that we are only showing 12 out of 24  
557 variants for brevity. In summary, the in situ measurements  
558 of A/M interface orientations as reported here showed  
559 excellent agreement with the phenomenological theory  
560 lending support to our transformation strain calculations.

### Comparison of Experimental Results and Theoretical Results

561  
562  
563 A compendium of the experimental results and the theo-  
564 retical predictions are shown in Figs. 18 and 19. The  
565 experimental results are given for NiTi13Hf and NiTi25Hf  
566 single and polycrystals. The experimental results are  
567 compared with theory for a number of single-crystal

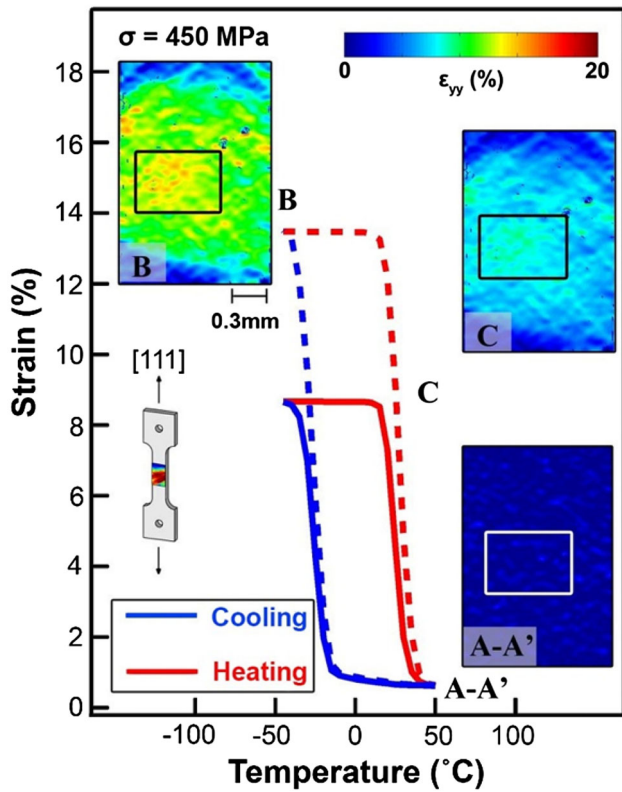
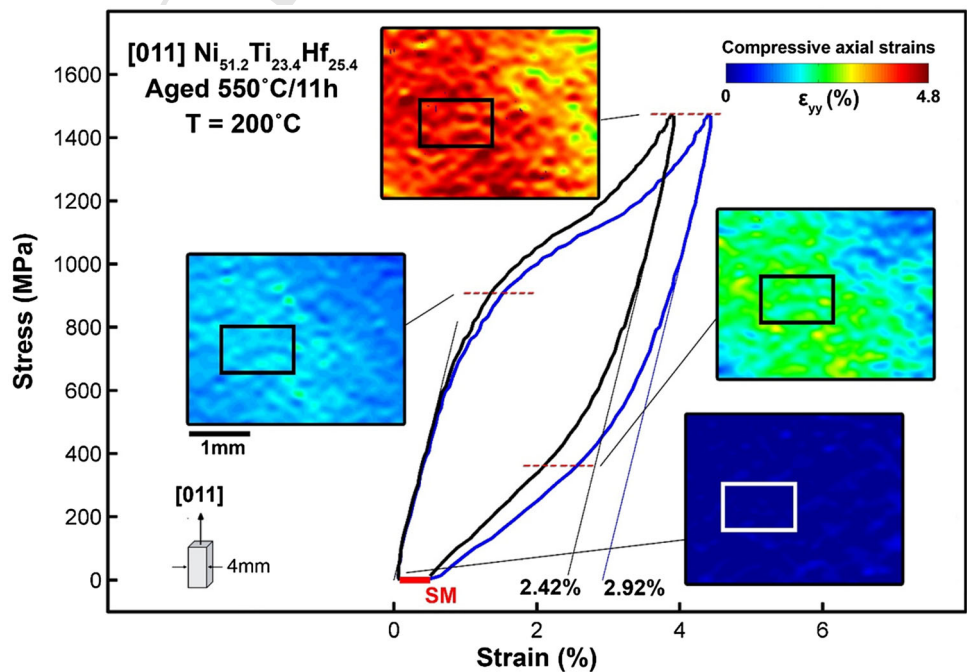


**Fig. 15** Isobaric strain–temperature results for the NiTi13Hf alloys oriented in [111] direction under tension. External applied stress is 450 MPa. The dashed line represents the results using the smaller domain marked with a rectangle

568 orientations. There are nearly 60 experiments conducted  
 569 providing an extensive experimental database. The exper-  
 570 imental results were obtained from three types of

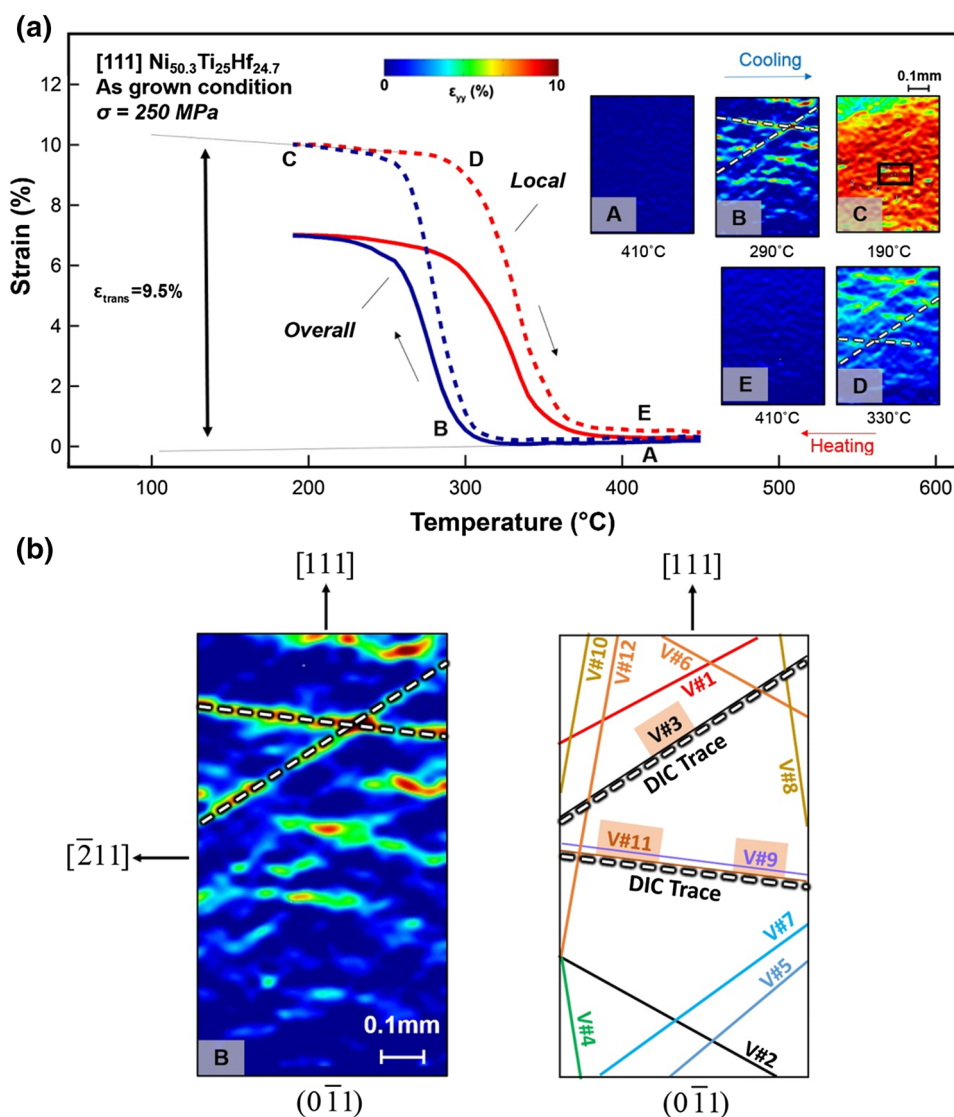
**Fig. 16** The superelastic behavior of [011] Ni<sub>51.2</sub>Ti<sub>23.4</sub>Hf<sub>25.4</sub> single crystals in compression at 200 °C is illustrated. The specimen was aged at 550 °C for 11 h. The local strain–strain behavior (blue curve) was obtained within the rectangular volume, while the overall strain measurement (black curve) was presented by averaging the entire DIC region (Color figure online)



571 experiments: (i) shape memory (deform below  $M_f$ , unload  
 572 to zero stress, and heat for recovery), (ii) superelasticity  
 573 (load and unload at constant temperature), and (iii) isobaric  
 574 temperature cycling (under constant stress). In the shape  
 575 memory experiments on NiTi13Hf, the specimens were  
 576 deformed at  $-30\text{ }^\circ\text{C}$  and at higher temperatures near  $50\text{ }^\circ\text{C}$   
 577 for superelasticity. The recoverable strains were in the  
 578 range 12–22%. The range of experimental results are  
 579 indicated with error bars. The specimens are from different  
 580 batches of single crystals with small variations in compo-  
 581 sition (in both Ni and Hf contents) which result in variation  
 582 of results. These results are very impactful because of the  
 583 large strains. The transformation strains in tension are very  
 584 high in [111] orientation with experimental results  
 585 exceeding the theoretical values in some cases. This is  
 586 possibly due to additional twinning modes that may be  
 587 recoverable beyond the phase transformation. The poly-  
 588 crystalline results fall below the [011] strain levels in  
 589 Fig. 18. In Fig. 19, the NiTi25Hf results are presented for  
 590 [011]-, [111]-, [3 4 14]-, and [001]-oriented single crystals.  
 591 All the results given are for compression, except the [111]  
 592 case which includes tensile results. To be more specific, the  
 593 compression results are shown for Ni<sub>51.2</sub>Ti<sub>23.4</sub>Hf<sub>25.4</sub> alloys.  
 594 The tensile results are illustrated for [111] Ni<sub>50.3</sub>Ti<sub>25</sub>Hf<sub>24.7</sub>  
 595 single crystals. Among the tensile database, the results of  
 596 the aged cases are marked as triangles. Note that the  
 597 temperatures in Fig. 19 are far higher than those in Fig. 18.

598 The most noteworthy results are the following: (i) in  
 599 isobaric experiments on [111] NiTi25Hf (at a constant  
 600 stress of 250 MPa) resulted in strain near 10%, (Fig. 16)  
 601 (ii) on [111] NiTi13Hf isobaric tension, the transformation

**Fig. 17** **a** Isobaric experiments on  $[111]$   $\text{Ni}_{50.3}\text{Ti}_{25}\text{Hf}_{24.7}$  single crystals showing local strains near 9.5% and transformation (austenite finish) temperatures are near 420 °C. External applied stress is tensile at 250 MPa. Strains for both the local (marked with a box on the figure) and global scale (the entire DIC area) are shown. **b** Comparison of DIC results and the traces of martensite variants showing activation of V#3, V#9, and V#11 (only 12 variants are shown for simplicity). Note that EBSD characterized the loading and side orientation of the sample



602 strain was as high as 14% (Fig. 15), and (iii) in superelasticity experiment on  $[111]$   $\text{NiTi13Hf}$  under compression, 603 the strain was near 7% (Fig. 14). 604

605 The experimental points are obtained using local strain 606 measurements via digital image correlation (DIC). The 607 details of DIC method can be found in [25, 48, 49]. Local 608 strains determined with DIC technique establish the maximum 609 transformation strains for the specific crystal orientation. The results presented represent the intrinsic 610 maximum transformation strain obtainable along a specific 611 crystal orientation. 612

613 The polycrystalline transformation strain is also shown 614 in Figs. 18 and 19 using a micromechanical model [50]. 615 The orientations of the grains are measured using electron 616 back scattering diffraction (EBSD). In the micromechanical 617 model, the transformed martensite is treated as an 618 inhomogeneity embedded in a grain. The internal stress is 619 calculated, upon averaging over multiple active variants,

and provides a measure of the overall stress. The overall 620 transformation strains are calculated by considering the 621 transforming inhomogeneity constrained by the surrounding 622 matrix. The grain orientations are measured with 623 EBSD and used as input to the model. In our case, it was 624 found that the polycrystalline grains favored the  $[011]$  625 orientation. An example of EBSD measurements and the 626 local deformation is shown in Fig. 20. The strain fields 627 obtained with DIC were successively overlapped and a 628 direct correlation between transformation strains and grain 629 orientation was then obtained for the polycrystalline 630 specimens. The largest strains were measured for those 631 grain orientations predominantly oriented along the  $[011]$  632 direction in compression. We note that the grain orientations 633 near  $[011]$  and  $[111]$  poles exhibit the highest shape 634 memory functionality for compression and tension, 635 respectively. The grains near the  $[001]$  pole exhibit small 636 strain values in both cases. 637

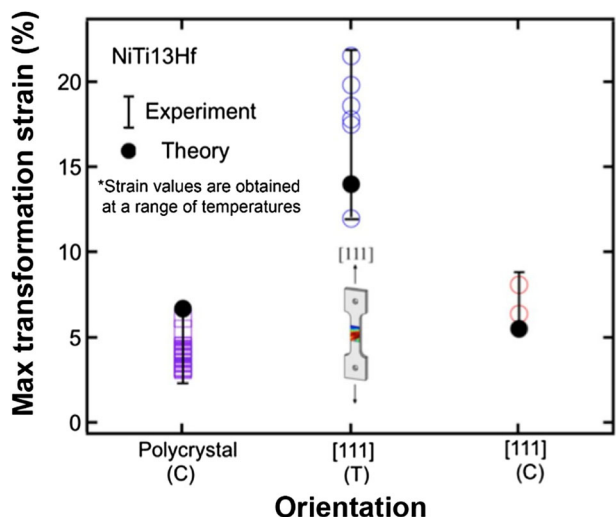


**Fig. 18** Maximum transformation strain for NiTi13Hf single crystals and polycrystalline alloy. The compressive results have been presented for polycrystalline and single crystalline oriented along [111] direction. The tensile results have been shown for [111] single crystals as well. The test results were obtained at a range of temperatures

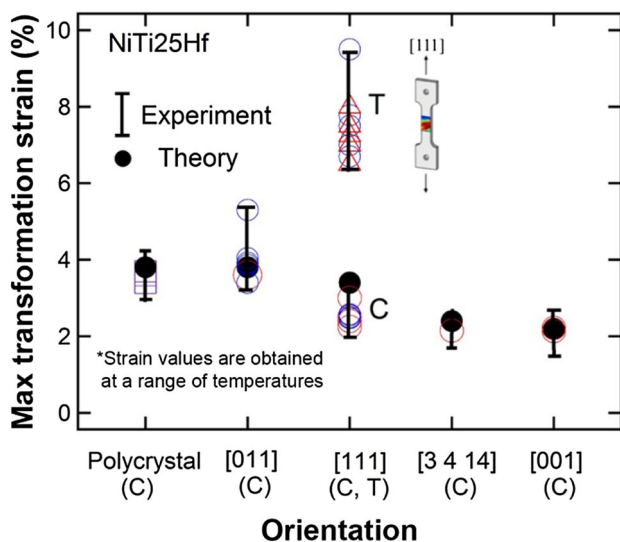


**Fig. 19** Maximum transformation strain for the NiTi25Hf polycrystalline alloy and several single crystals. The compression results are shown for Ni<sub>51.2</sub>Ti<sub>23.4</sub>Hf<sub>25.4</sub> alloys. The tensile results of Ni<sub>50.3</sub>Ti<sub>25.7</sub>Hf<sub>24.7</sub> single crystals oriented in [111] direction are presented. Among the tensile database, the results of the aged cases are illustrated as triangles. The test results were obtained at a range of temperatures

638 **Discussion of Results**

639 We note that the stress–strain curves for the [111] compression case (Fig. 14) show an inhomogeneous martensitic transformation. A stress plateau typically identified with SMA alloys ensures transformation, while an ascending stress–strain curve reaches the slip stress which results in irreversibility. In this latter case, multiple

645 martensite plates are nucleated which elevates the stress upon deformation. Fortunately, the hardening level (due to possible martensite–slip or martensite–martensite interaction), i.e., the slope, is not sufficiently high to elevate the stresses to create dislocation slip at the macroscale. Our recent DFT calculations point to very high critical shear stress levels for slip in NiTiHf alloys (CRSS = 614 MPa for NiTi25Hf case), and therefore, these alloys can accommodate higher internal stresses compared to binary NiTi. Austenite-yielding Schmid factors are near 0.5 for the prevailing <100> {110} slip system [51] [52] for both [011] and [111] orientations. It is the high critical slip stress that allows orientations such as [011] and [111] to achieve high strains without gross slip deformation. Based on the stress–strain curves, the uniaxial flow stresses, near the *M<sub>d</sub>* temperature, are 1100 MPa and 900 MPa for NiTi13Hf and NiTi25Hf, respectively. These values are higher than the 500 MPa level for binary NiTi [53]. The *M<sub>d</sub>* temperature is the temperature above which slip dominates. The *M<sub>d</sub>* temperatures are 110 and 380 °C for NiTi13Hf and NiTi25Hf, respectively. A linear extrapolation of the high-temperature results should be made for the NiTi25Hf case to compare these results at the same temperature (this results in flow stress exceeding 1600 MPa for the NiTi25Hf case). We note that the critical stress for austenite to martensite transformation is lower than the slip stresses for NiTiHf alloys. When the *A<sub>f</sub>* temperature is of the same order as *M<sub>d</sub>* temperature, this would limit the superelastic window in NiTi25Hf compared to NiTi13Hf. At the same time, the isobaric shape memory functionality of NiTi25Hf is extraordinary, and not affected by the closeness of *A<sub>f</sub>*–*M<sub>d</sub>*, as shown in Fig. 17.

677 Martensite detwinning can result in a single martensite variant that is dominant [21]. The detwinning strain is calculated as an additional transformation strain component. The detwinning strain in tension in NiTi-based alloys is considered to be significant. We have considered all possible twin systems in our calculations and focused on the Type I twinning observed in experiments. Considering Fig. 15, we note that the transformation strain locally is reaching 13% and this value is consistent with Table 4—row 3. We selected the [111] orientation to give the highest transformation strain in tension based on theory, and our results confirm this finding. Reorientation of martensite occurs as further detwinning develops. In this case, martensite plates containing Type I twins migrate under tensile deformation. In contrast, under compression, this mechanism was not favored resulting in smaller strain magnitudes. We note that the detwinning process can be curtailed due to grain boundaries in polycrystalline alloys.

695 The results (Fig. 14) show that the unloading modulus of the martensite is higher than the austenite elastic modulus in NiTiHf alloys. This is a topic of current importance

**Fig. 20** EBSD and experimental strain map obtained with high-resolution digital image correlation strain measurements under compression. The strain measurements show that the grains which undergo the largest strains are those orientated close to the [011] orientation. The orientations close to [111] also undergo high strains which are comparable to the [001]-oriented grains

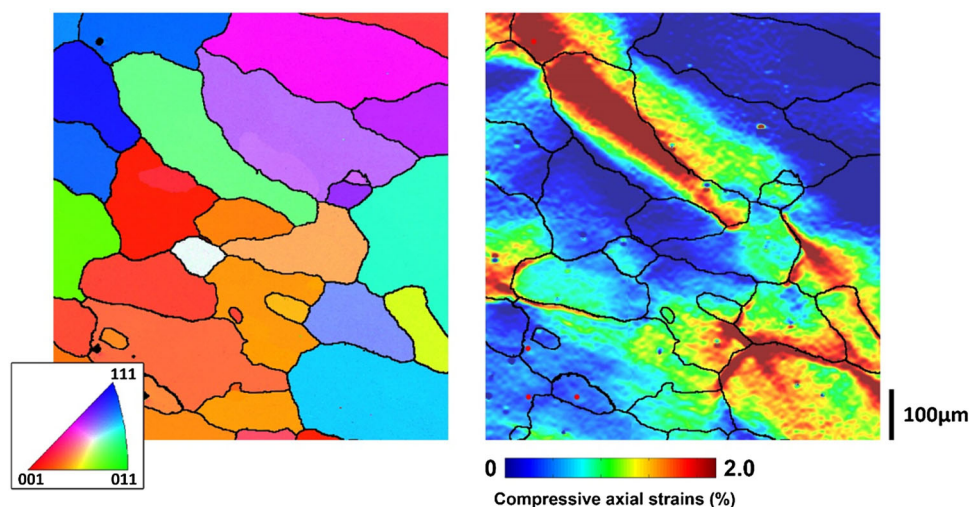


**Table 4** Theoretical tensile transformation strains based on cubic to monoclinic model

	[111] Single crystal			[011] Single crystal			[001] Single crystal		
	(011)-Type I CVP strain (%)	(011)-Type I CVP and detwinning strain (%)	LDT strain (%)	(011)-Type I CVP strain (%)	(011)-Type I CVP and detwinning strain (%)	LDT Strain (%)	(011)-Type I CVP strain (%)	(011)-Type I CVP and detwinning strain (%)	LDT strain (%)
NiTi* (HS)	5.11	10.27	9.79	4.07	8.75	8.40	2.72	2.72	2.68
NiTi6.25Hf (HS)	6.15	12.30	11.63	4.52	9.99	9.54	3.16	3.16	3.11
NiTi12.5Hf (HS)	5.15	13.38	12.59	3.49	10.16	9.69	1.87	1.87	1.85
NiTi15Hf (DH)	8.81	17.5	16.17	6.04	8.39	10.66	2.76	2.76	2.73
NiTi20Hf (HK)	10.07	19.69	18.06	7.17	9.95	11.42	2.92	2.92	2.80
NiTi20Hf (OB)	12.02	20.85	19.04	8.09	10.84	11.95	3.79	3.79	3.72
NiTi20Hf (DH)	9.36	19.34	17.76	6.77	9.60	11.31	2.63	2.63	2.59
NiTi20Hf (AS)	9.70	19.60	17.95	6.87	9.72	11.44	2.84	2.84	2.80
NiTi25Hf (HS)	13.42	19.83	18.93	9.70	11.61	11.53	3.15	3.15	3.10

Note that orientations near [111] pole produce strains as high as 19% in tension for NiTi25Hf

\* CVP and CVP detwinning strain for NiTi are for [001]-Type II twin

698 because there is a misconception about the moduli of the  
699 two phases. As noted in our previous work [54], the  
700 martensite moduli are higher than austenite moduli. The  
701 higher martensite modulus creates favorable fatigue crack  
702 growth resistance as noted in early work [49].

703 The constant stress levels for thermal cycling experi-  
704 ments in NiTi [47] were mostly less than 200 MPa, and at  
705 higher stress levels, permanent inelastic deformation

occurs. The response of strain–temperature is highly non-  
linear as seen in Figs. 15 and 17 but at much higher stresses  
(450 MPa) in NiTi13Hf and 250 MPa in NiTi25Hf. These  
nonlinear strain–temperature curves point to the strong role  
of variant–variant interaction, the high levels of stored  
elastic energy and result in a more gradual transformation  
upon cooling [47]. Also, a wider hysteresis is noted in  
NiTiHf alloys (near 60 °C in Figs. 15 and 17) compared to

714 NiTi, and depending on the application (actuator vs  
715 damping), small or large hysteresis may be beneficial.

716 The experimental results clearly show a strong orienta-  
717 tion dependence (Figs. 18, 19). The orientations of most  
718 interest are the [111] and [011] cases. It is remarkable to  
719 observe how the addition of Hf to 25% results in a dramatic  
720 upswing in the [111] compression theory case (Fig. 3b)  
721 which is supported by experiments showing unusually high  
722 strains in [111] (Fig. 14). Although the [001] pole has been  
723 shown to be of interest in NiTi alloys [22] because of low  
724 Schmid factor for slip and good transformation strains in  
725 compression, the theoretical predictions showed that the  
726 transformation strain in [001] direction in fact decreased  
727 with increasing Hf content. The experimental results  
728 summarized in Fig. 19 confirm that [001] pole results in  
729 very small transformation strains.

730 The Clausius-Clapeyron equation has been established  
731 based on the experiments, the  $d\sigma/dT$  values pointed to  
732 14 MPa/°C for NiTi13Hf ([011] orientation), while the  
733 slope was 10 MPa/°C for NiTi25Hf. The criteria for  
734 superelasticity [55] have been shown to be favored with a  
735 lower thermal hysteresis,  $A_f-M_s$ , lower  $d\sigma/dT$ , and lower  
736 transformation stress relative to slip stress. For NiTiHf, the  
737 hysteresis levels exceed the values for NiTi, while a higher  
738 slip resistance facilitates superelasticity. In that regard, the  
739 NiTiHf alloys are similar to high Ni 51.5Ni–Ti alloys  
740 where superelasticity can readily occur [56]. The main  
741 difference is that in 51.5Ni–Ti alloys, the transformation  
742 strains are less than 3% unlike the NiTiHf alloys where the  
743 strains are exceeding 10%. Therefore, the NiTiHf alloys  
744 present unique properties in the SMA field.

## 745 Conclusions

746 The work supports the following:

- 747 1. The results show the considerable promise of the NiTiHf  
748 alloys. The results point to transformation strains as high  
749 as 12% for the NiTi13Hf which can be suited for  
750 applications requiring ultra-high strains. Austenite fin-  
751 ish temperatures exceeding 420 °C were measured for  
752 the 25Hf composition with transformation strain levels  
753 near 10% in tension. The functionality at such high  
754 temperatures opens new technological possibilities.
- 755 2. The level of theoretical transformation strains based on  
756 the cubic to monoclinic model is in general agreement  
757 with experimental results on NiTiHf alloys with  
758 increasing Hf content. The experimental results show  
759 that transformation strains were found to be highest in  
760 [111] tension for NiTi13Hf and NiTi25Hf alloys,  
761 respectively. Therefore, suitable texturing treatments  
762 can produce very favorable alloys in tension. The habit

plane orientation obtained from DIC is in perfect  
agreement with the predicted habit plane variant from  
theory providing independent support on the calcula-  
tions of lattice constants and the phenomenological  
theory.

3. The theoretical transformation strains shift to higher  
levels as Hf content increases. This is ultimately related  
to the changes in the lattice constants (most prominently  
the monoclinic angle is approaching 105.4° for the 25Hf  
case) induced by the increase of Hf content. The  
polycrystalline alloy transformation strains were also  
predicted using the EBSD/X-ray diffraction results and a  
micromechanical analysis. The polycrystal compression  
specimens have preferred <011> texture and showed  
experimental (and theoretical) levels comparable to  
<011> single crystals tested in compression. The  
transformation strains levels in compression are higher  
than 6% which exceeds binary NiTi alloys.
4. Based on the theoretical results, the detwinning strain  
is much more significant for deformation under tension  
than under compression. Theoretical transformation  
strains for detwinned martensite and lattice deforma-  
tion theory are in general agreement. Because of the  
high slip resistance of NiTiHf alloys, the transforma-  
tion can proceed even at high stresses without the  
propensity of gross slip.
5. The lattice constants measured with selected area  
diffraction using TEM and the DFT results are in  
excellent agreement and point to large monoclinic  
angles which result in large transformation strains. The  
TEM results confirm the presence of Type I transfor-  
mation twins and (001) compound twinning. The twin  
types are the same in aged and solutionized crystals.  
The results point to blocky precipitates as opposed to  
lenticular ones rich in Ni and Hf.

**Acknowledgements** The work is supported by a National Science  
Foundation grant NSF CMMI-1333884 which is gratefully  
acknowledged. Professor Nishida acknowledges the Grant No.  
26249090 from the Japanese Society for the Promotion of Science.  
Prof. Chumlyakov was supported by RSF 14-29-00012.

## Appendix 1: Lattice Constant Determination by Density Functional Theory and Transformation of NiTi<sub>25</sub>Hf

Lattice constant calculations are demonstrated for the 25%  
Hf case in Fig. 21. The first-principles Density Functional  
Theory (DFT) calculations—Vienna ab initio Simulations  
Package (VASP) with the projector augmented wave  
(PAW) method and the generalized gradient approximation  
(GGA) [57, 58] were performed. In our calculations, we

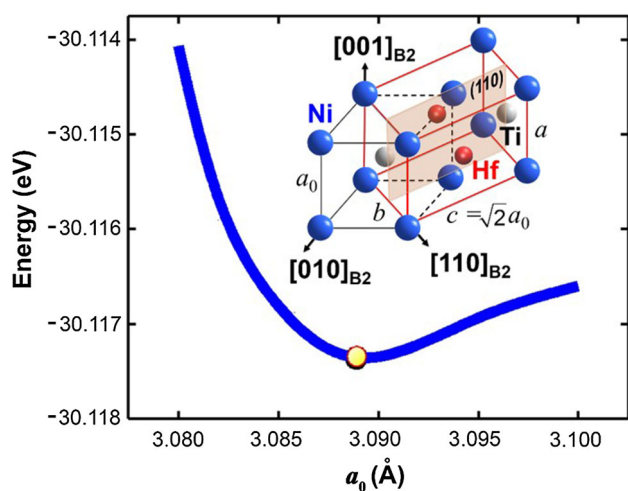


**Fig. 21** Energy minimization to obtain the lattice constant of B2 NiTi25Hf. The total energy is reported for 4 atoms in a cell

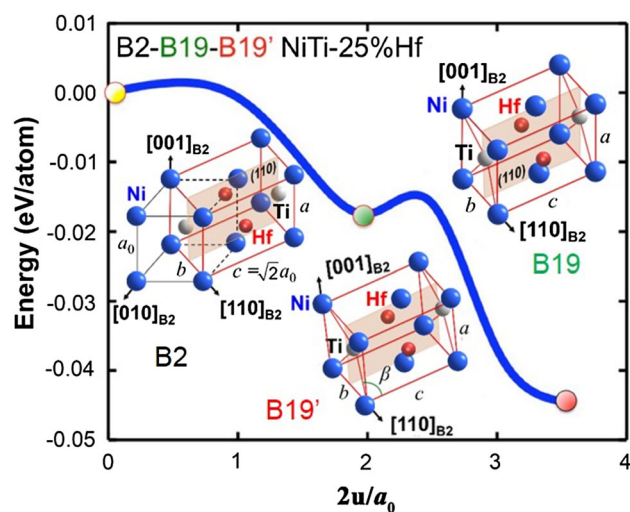


**Fig. 22** B2–B19–B19' transformation path of NiTi25Hf (schematics not to scale). The austenitic crystal structure is B2, and energy/atom is given with respect to B2 energy.

812 used a  $9 \times 9 \times 9$  Monkhorst–Pack  $k$ -point meshes for the  
813 Brillouin-zone integration to ensure the convergence of  
814 results. Ionic relaxation was performed by a conjugate  
815 gradient algorithm. The energy cut-off of 360 eV was used  
816 for the plane-wave basis set. The total energy was con-  
817 verged to less than  $10^{-5}$  eV per atom. For lattice constant  
818 determination, a full internal atom relaxation was allowed  
819 for minimizing the total energy of the crystal. For cubic  
820 crystal, we obtained the energy variation of the crystal with  
821 respect to different lattice parameters in our simulations.  
822 The equilibrium lattice constant corresponding to the  
823 minimum structural energy (for austenite) was obtained as  
824 3.089 Å. The lattice constants obtained through DFT cal-  
825 culations which are within 2% of the experimentally  
826 observed value. In case of monoclinic NiTiHf, we under-  
827 took energy minimization with respect to each of the lattice  
828 parameters sequentially. The orthorhombic structure can be  
829 derived from the cubic structure by allowing lattice  
830 parameters to change for the constant monoclinic angle.  
831 This deformation can be expressed in terms of the lattice  
832 constant ratios  $b/c$  and  $a/c$  for a fixed volume.

833 While the martensitic transformation in equiatomic NiTi  
834 has been well studied, that of the NiTiHf is still lacking.  
835 We note that the transformation from B2 to B19' phase  
836 occurs through an intermediate B19 phase during which the  
837 lattice constants and monoclinic angle change. Here, we  
838 present the complete energy pathway associated with the  
839 martensitic transformation in NiTi25Hf. It is proposed that  
840 B2–B19 transformation occurs by the application of a  
841  $\langle 110 \rangle \{110\}$  basal bilayer shear and shuffle [59]. Further  
842  $\langle 110 \rangle \{001\}$  nonbasal shear transforms the B19–B19'  
843 structure. The shear displacements are shown as horizontal  
844 axis in Fig. 22. We observe that during the transformation  
845 from B19 to B19', the  $c$ -axis elongation is prominent. Our

846 first-principles energy calculations confirm that B19' has a  
847 lower energy compared to B19 structure by 25 meV/atom.  
848 The energy transformation barrier from B2 structure to  
849 B19 requires overcoming a barrier of 2 meV/atom and  
850 B19–B19' close to 10 meV/atom. As stated earlier, the  
851 energy barrier between B19 and B19' is small, raising the  
852 possibility that B19 could exist in micro-domains. This is  
853 beyond the scope of this paper.

## References

- 854 1. Duerig TW, Melton K, Stockel D, Wayman C (1990) Engineer-  
855 ing aspects of shape memory alloys. Butterworth-Heinemann,  
856 Rushden
- 857 2. Miyazaki S, Otsuka K, Suzuki Y (1981) Transformation pseu-  
858 doelasticity and deformation behavior in a Ti-50.6at%Ni alloy.  
859 Scr Metall 15:287–292
- 860 3. Hamilton RF, Sehitoglu H, Chumlyakov Y, Maier HJ (2004)  
861 Stress dependence of the hysteresis in single crystal NiTi alloys.  
862 Acta Mater 52:3383
- 863 4. Stradel B, Ohashi S, Ohtsuka H, Miyazaki S, Ishihara T (1995)  
864 Effect of mechanical cycling on the pseudoelasticity character-  
865 istics of TiNi and TiNiCu alloys. Mater Sci Eng A 203:187–196
- 866 5. Lagoudas DCE (2010) Shape memory alloys. Springer, Berlin
- 867 6. Chowdhury P, Sehitoglu H (2016) Significance of slip propensity  
868 determination in shape memory alloys. Scr Mater 119:82–87
- 869 7. Angst RD, Thoma EP, Kao YM (1995) The effect of hafnium  
870 content on the transformation temperatures of Ni<sub>[49]</sub>Ti<sub>[51-x]</sub>Hf<sub>[x]</sub>  
871 shape memory alloys. EDP Sciences, Les Ulis
- 872 8. Han XD, Zou WH, Wang R, Zhang Z, Yang DZ (1996) Structure  
873 and substructure of martensite in a Ti<sub>36.5</sub>Ni<sub>48.5</sub>Hf<sub>15</sub> high tem-  
874 perature shape memory alloy. Acta Mater 44:3711–3721
- 875 9. Potapov PL, Shelyakov AV, Gulyaev AA, Svistunov EL, Mat-  
876 veeva NM, Hodgson D (1997) Effect of Hf on the structure of  
877 Ni–Ti martensitic alloys. Mater Lett 32:247–250
- 878 10. Wu KH, Pu ZJ, Gao Y, Wayman CM (1998) Study of NiTi–Hf  
879 and NiTi–Zr high-temperature shape memory alloys. Proceedings  
880 of the 1996 international conference on displacive phase  
881  
882

- transformations and their applications in materials engineering, May 8, 1996–May 9, 1996. Minerals, Metals & Materials Soc (TMS), Urban, pp 285–290
11. Zheng YF, Cai W, Zhang JX, Wang YQ, Zhao LC, Ye HQ (1998) High-resolution electron microscopy study on the substructure of Ti–Ni–Hf B19' Martensite. *Mater Lett* 36:142–147
  12. Thoma PE, Boehm JJ (1999) Effect of composition on the amount of second phase and transformation temperatures of  $Ni_xTi_{90-x}Hf_{10}$  shape memory alloys. *Mater Sci Eng A* 273–275:385–389
  13. Meng XL, Zheng YF, Wang Z, Zhao LC (2000) Effect of aging on the phase transformation and mechanical behavior of  $Ti_{36}Ni_{49}Hf_{15}$  high temperature shape memory alloy. *Scr Mater* 42:341–348
  14. Dalle F, Perrin E, Vermaut P, Masse M, Portier R (2002) Interface mobility in  $Ni_{49.8}Ti_{42.2}Hf_8$  shape memory alloy. *Acta Mater* 50:3557
  15. Santamarta R, Seguí C, Pons J, Cesari E (1999) Martensite stabilisation in  $Ni_{50}Ti_{32.2}Hf_{17.7}$ . *Scr Mater* 41:867–872
  16. Wang J, Sehitoglu H (2014) Modelling of martensite slip and twinning in NiTiHf shape memory alloys. *Philos Mag* 94:2297–2317
  17. Wang J, Sehitoglu H, Maier HJ (2014) Dislocation slip stress prediction in shape memory alloys. *Int J Plast* 54:247–266
  18. Ma J, Karaman I, Noebe RD (2010) High temperature shape memory alloys. *Int Mater Rev* 55:257–315
  19. Stebner AP, Bigelow GS, Jin Y, Shukla DP, Saghalian SM, Rogers R et al (2014) Transformation strains and temperatures of a nickel–titanium–hafnium high temperature shape memory alloy. *Acta Mater* 76:40–53
  20. Karaca H, Saghalian S, Basaran B, Bigelow G, Noebe R, Chumlyakov Y (2011) Compressive response of nickel-rich NiTiHf high-temperature shape memory single crystals along the [111] orientation. *Scr Mater* 65:577–580
  21. Sehitoglu H, Hamilton R, Canadinc D, Zhang XY, Gall K, Karaman I et al (2003) Detwinning in NiTi alloys. *Metall Mater Trans A* 34:5
  22. Sehitoglu H, Karaman I, Anderson R, Zhang X, Gall K, Maier H et al (2000) Compressive response of NiTi single crystals. *Acta Mater* 48:3311–3326
  23. Miyazaki S, Kimura S, Takei F, Miura T, Otsuka K, Suzuki Y (1983) Shape memory effect and pseudoelasticity in a Ti–Ni single crystal. *Scr Metall* 17:1057–1062
  24. Matsumoto O, Miyazaki S, Otsuka K, Tamura H (1987) Crystallography of martensitic transformation in TiNi single crystals. *Acta Metall* 35:2137–2144
  25. Wu Y, Patriarca L, Li G, Sehitoglu H, Soejima Y, Ito T et al (2015) Shape memory response of polycrystalline  $NiTi_{12.5}Hf$  alloy: transformation at small scales. *Shap Mem Superelast* 1:387–397
  26. Thoma P, Zhang C, Boehm JJ, Zee RH (1997) The effect of hafnium content and cycling under an applied axial stress on the creep and martensite strain of NiTi based shape memory alloy wires. *J Phys IV Fr* 7:C5-483–C5-8
  27. Santamarta R, Seguí C, Pons J et al (1999) Martensite stabilisation in  $Ni_{[50]}Ti_{[32.2]}Hf_{[17.7]}$ . Elsevier, Kidlington
  28. Kockar B, Karaman I, Kim J, Chumlyakov Y (2006) A method to enhance cyclic reversibility of NiTiHf high temperature shape memory alloys. *Scr Mater* 54:2203–2208
  29. Profiles Material (2010) Materials and design, 2nd edn. Butterworth-Heinemann, Oxford, pp 194–249
  30. Chantz MD, David AM (2012) Thermomechanical training and characterization of Ni–Ti–Hf and Ni–Ti–Hf–Cu high temperature shape memory alloys. *Smart Mater Struct* 21:065020
  31. Coughlin DR, Phillips PJ, Bigelow GS, Garg A, Noebe RD, Mills MJ (2012) Characterization of the microstructure and mechanical properties of a  $50.3Ni_{-29.7}Ti_{-20}Hf$  shape memory alloy. *Scr Mater* 67:112–115
  32. Santamarta R, Arróyave R, Pons J, Evirgen A, Karaman I, Karaca H et al (2013) TEM study of structural and microstructural characteristics of a precipitate phase in Ni-rich Ni–Ti–Hf and Ni–Ti–Zr shape memory alloys. *Acta Mater* 61:6191–6206
  33. Wang J, Sehitoglu H (2014) Dislocation slip and twinning in Ni-based L12 type alloys. *Intermetallics* 52:20–31
  34. Gall K, Sehitoglu H, Chumlyakov YI, Kireeva IV (1999) Tension–compression asymmetry of the stress–strain response in aged single crystal and polycrystalline NiTi. *Acta Mater* 47:1203–1217
  35. Carroll J, Abuzaid W, Lambros J, Sehitoglu H (2010) An experimental methodology to relate local strain to microstructural texture. *Rev Sci Instrum* 81:083703
  36. Efstathiou C, Sehitoglu H, Carroll J, Lambros J, Maier HJ (2008) Full-field strain evolution during intermartensitic transformations in single-crystal NiFeGa. *Acta Mater* 56:3791–3799
  37. Patriarca L, Wu Y, Sehitoglu H, Chumlyakov YI (2016) High temperature shape memory behavior of  $Ni_{50.3}Ti_{25}Hf_{24.7}$  single crystals. *Scr Mater* 115:133–136
  38. Wu Y, Patriarca L, Sehitoglu H, Chumlyakov Y (2016) Ultrahigh tensile transformation strains in new  $Ni_{50.5}Ti_{36.2}Hf_{13.3}$  shape memory alloy. *Scr Mater* 118:51–54
  39. Patriarca L, Sehitoglu H, Panchenko EY, Chumlyakov YI (2016) High-temperature functional behavior of single crystal  $Ni_{51.2}Ti_{23.4}Hf_{25.4}$  shape memory alloy. *Acta Mater* 106:333–343
  40. Otsuka K, Sawamura T, Shimizu K (1971) Crystal structure and internal defects of equiatomic TiNi martensite. *Phys Status Solidi A* 5:457
  41. Karaca HE, Saghalian SM, Ded G, Tobe H, Basaran B, Maier HJ et al (2013) Effects of nanoprecipitation on the shape memory and material properties of an Ni-rich NiTiHf high temperature shape memory alloy. *Acta Mater* 61:7422–7431
  42. Benafan O, Garg A, Noebe RD, Bigelow GS, Padula Ii SA, Gaydos DJ et al (2014) Mechanical and functional behavior of a Ni-rich  $Ni_{50.3}Ti_{29.7}Hf_{20}$  high temperature shape memory alloy. *Intermetallics* 50:94–107
  43. Saburi T, Nenno S (1981) The shape memory effect and related phenomena. In: Solid to solid phase transformations. pp 1455–1479
  44. Bhattacharya K (2003) Microstructure of martensite: why it forms and how it gives rise to the shape-memory effect. Oxford University Press, Oxford
  45. Nishida M, Nishiura T, Kawano H, Inamura T (2012) Self-accommodation of B19' Martensite in Ti–Ni shape memory alloys—part I. Morphological and crystallographic studies of the variant selection rule. *Philos Mag* 92:2215–2233
  46. Nishida M, Wayman CM, Chiba A (1988) Electron microscopy studies of the martensitic transformation in an aged Ti–51 at %Ni shape memory alloy. *Metallography* 21:275–291
  47. Sehitoglu H, Hamilton R, Maier HJ, Chumlyakov Y (2004) Hysteresis in NiTi alloys. EDP Sciences, Frejus, p 3
  48. Patriarca L, Sehitoglu H (2015) High-temperature superelasticity of  $Ni_{50.6}Ti_{24.4}Hf_{25.0}$  shape memory alloy. *Scr Mater* 101:12–15
  49. Wu Y, Ojha A, Patriarca L, Sehitoglu H (2015) Fatigue crack growth fundamentals in shape memory alloys. *Shap Mem Superelast* 1:18–40
  50. Gall K, Sehitoglu H (1999) The role of texture in tension–compression asymmetry in polycrystalline NiTi. *Int J Plast* 15:69–92
  51. Surikova NS, Chumlyakov YI (2000) Mechanisms of plastic deformation of the titanium nickelide single crystals. *Phys Met Metall* 89:196
  52. Ezaz T, Wang J, Sehitoglu H, Maier HJ (2013) Plastic deformation of NiTi shape memory alloys. *Acta Mater* 61:67–78
  53. Gall K, Sehitoglu H, Chumlyakov YI, Kireeva IV, Maier HJ (1999) The influence of aging on critical transformation stress

- 1015 levels and martensite start temperatures in NiTi: part II-discus- 1024  
 1016 sion of experimental results. *Trans ASME J Eng Mater Technol* 1025  
 1017 121:28–37 1026  
 1018 54. Wang J, Sehitoglu H (2014) Martensite modulus dilemma in 1027  
 1019 monoclinic NiTi-theory and experiments. *Int J Plast* 61:17–31 1028  
 1020 55. Liu Y, Galvin SP (1997) Criteria for pseudoelasticity in near- 1029  
 1021 equiatomic NiTi shape memory alloys. *Acta Mater* 45:4431–4439 1030  
 1022 56. Sehitoglu H, Jun J, Zhang X, Karaman I, Chumlyakov Y, Maier 1031  
 1023 HJ et al (2001) Shape memory and pseudoelastic behavior of 1032  
 51.5%Ni–Ti single crystals in solutionized and overaged state. 1033  
*Acta Mater* 49:3609–3620  
 57. Kresse G, Furthmüller J (1996) Efficient iterative schemes for  
 ab initio total-energy calculations using a plane-wave basis set.  
*Phys Rev B* 54:11169–11186  
 58. Kresse G, Hafner J (1993) Ab initio molecular dynamics for  
 open-shell transition metals. *Phys Rev B* 48:13115  
 59. Wang J, Sehitoglu H (2012) Resolving quandaries surrounding  
 NiTi. *Appl Phys Lett* 101:081907

REVISIED PROOF